EXPLOSIVE SHOCK-WAVE CONSOLIDATION OF METAL AND CERAMIC POWDERS

Marc A. Meyers, Naresh N. Thadhani*, and Li-Hsing Yu

*CENTER FOR EXPLOSIVES TECHNOLOGY RESEARCH

and

DEPARTMENT OF MATERIALS AND METALLURGICAL ENGINEERING

NEW MEXICO INSTITUTE OF MINING AND TECHNOLOGY

SOCORRO, NEW MEXICO 87801 (U.S.A.)

ABSTRACT

Shock-wave consolidation utilizing explosives as the energy source is a technique that has considerable potential for bonding powders of very hard materials (e.g., diamond, boron nitride) and of alloys that have been produced by rapid solidification and that cannot undergo prolonged thermal excursions during processing. The experimental techniques used by the authors and co-workers at the New Mexico Institute of Mining and Technology are presented. The various fixtures, with their intended applications and limitations, are described. These fixtures use room temperature and high-temperature cylindrical and plate configuration for larger components, and capsules containing the powders for smaller components (such as cutting tool bits). The microstructures produced by shock-wave processing of the powders are discussed. They consist, in metallic systems, of molten and rapidly solidified interparticle regions that are responsible for bonding, and the particle interiors that undergo shock hardening. In ceramic systems, the process of bonding seems to be solid state, and the collapse of the interparticle voids takes place by plastic deformation or crushing of parts of the particles, with rebonding. The mechanical properties of shock consolidated materials are reviewed. The principal limitations of this technology, cracking and net shape capability, are presented and the economic feasibility and scale-up methodology are discussed.

1. INTRODUCTION

Shock consolidation of powders is a one-stage densification/bonding process which presents potential for rapidly-solidified powders, and very hard and difficult-to-consolidate ceramics. This dynamic form of powder consolidation, which involves a very rapid and intense deposition of shock energy at powder particle surfaces resulting in interparticle bonding, has been known for over twenty years. Nevertheless, there is no commercial application of this process in the United States, except in the synthesis of diamond [1]. The production of the wurtzite form of boron nitride in Japan by shock energy is a modest industrial effort[2]. There are reports of extensive industrial applications of shock processing of powders in the U.S.S.R.[3,4]. Chapter ____ of this book$ details the Soviet work in the area.

The production of rapidly solidified metal powders and the need for hard ceramic cutting tools have revived the interest in this "exotic" consolidation process. Rapidly solidified powders, in particular, have been identified as materials possessing highly refined microstructures and at the same time being free from segregational problems[5]. However, conventional methods for consolidating both metal and ceramic powders involve prolonged thermal excursions; consequently, the resulting microstructure is coarser than that of the starting powder.

Shock-wave consolidation of powders is a technique that avoids prolonged heating, and can be used for producing bulk

solids in the form of disks, plates, cylinders, tubes, and cones. The basic mechanism by which consolidation is achieved as a shock wave passes through a porous medium is either by one or both of the following: (a) deformation and high-velocity impact of particles, filling the interstices, breaking down surface oxides, leading to heating and melting of particle near-surface material and subsequent welding; (b) deformation and fracture of particles, filling interstices, cleansing of surfaces, preferential heating of particle surfaces leading to partial melting and welding or solid-state-diffusional bonding. While the first mechanism seems to apply to metals, the second one is more prevalent in ceramics. Shock consolidation of powders has been recently reviewed by Gourdin[6] and by an NMAB study[7]. A number of papers can also be found in the Proceedings of the 1985 EXPLOMET International Conference[8].

In this article, four aspects of shock-wave consolidation will be discussed. First, the powder compaction experimental techniques used by the authors and co-workers will be presented with their respective merits and limitations. Second, the different rapidly solidified alloys and ceramics consolidated at the Center for Explosives Technology Research (New Mexico Institute of Mining and Technology) will be discussed. Third, the microstructural characteristics and the mechanical properties of the compacts will be presented. Fourth, the limitations of shock consolidation, problems with scale-up, and the economics of the process will be briefly discussed.

2. EXPERIMENTAL TECHNIQUES

2.1 Fundamental Equations.

Shock consolidation requires the very rapid collapse of the gaps between the particles as well as the rapid deposition of energy at the particle surfaces. These processes need to be close to adiabatic; if slow, heat transfer to the interior of the particles and surrounding will radically change the process. This ultra rapid deformation and energy deposition is accomplished in time durations of microseconds and fractions there-of by the passage of a shock wave through the powders. The amplitude of the shock wave has to be sufficient to bond the powders, but should not be so high as to produce excessive melting and cracking on subsequent reflections. The selection of the shock pressure required to effect the shock consolidation is often a matter of judgment and experimentation. Nevertheless, some guidelines can be established and Fig. 1 shows, in a very schematic way, that the shock pressure is related to the hardness of the starting powders. Other parameters are also important:

*initial porosity of powders

*melting temperature

*atomic bonding (metallic, ionic, or covalent)

*shape and size of particles

*surface contamination of powders

However, hardness seems to be of considerable importance, and is the principal determiner of the needed pressure.

In the design of the system, methods for calculation of the pressure pulse are important. A first, "engineering" calculation of pressure, strictly applicable only in plane, one-dimensional systems, serves as a design criterion. These "engineering" calculations should be complemented by computer predictions using hydrocodes. Two-dimensional hydrocodes are necessary to understand the complex wave propagation patterns within the powder containers. Some predictions from codes are presented throughout this chapter. The fundamental equations of shock physics and how they relate to powders will be presented below. Figure 2(a) shows a material at a pressure P_o, with an internal energy E, and a specific volume V_o (density $\rho_o = (1/V_o)$). A shock wave traveling from left to right, raises these values to P, E, V (density $\rho = 1/V$). This shock wave propagates at a velocity U_s and the individual particles propagate at a velocity U_p. The equations of conservation of mass, momentum, and energy are, respectively:

$$\rho (U_s - U_p) = \rho_o U_s \tag{1}$$

$$P = \rho_o U_s U_p \tag{2}$$

$$E = (1/2) P [1/\rho_o - 1/\rho] \tag{3}$$

By application of these equations and of a fourth equation, called equation of state of the material, it is possible to determine all shock-wave parameters, once one of them is set. The equation of state for the powder is the Mie-Gruneisen equation:

$$P = P_H + \rho \gamma (E - E_H) \tag{4}$$

Where P_H and E_H are the pressure and internal energy of the solid material, P and E are the corresponding values for the powder, and γ is the Gruneisen ratio. The detailed procedure on how to

obtain the shock parameters is described in detail by Meyers and Wang[9]. As an example, the pressure versus specific volume curves shown in Figure 2(b) have been generated by the application of equations 1 through 4, for the alloy Inconel 718 (a nickel-base superalloy).

From the Hugoniot relationships for a certain material (curves analogous to the ones shown in Fig. 2(b)) and by selecting a desired pressure, it is possible to determine the dimensions and energy input of the system required. This will be shown in the following sections.

There are several means of depositing on the powder surface the energy required for shock consolidation. These are:

* detonation of explosive in direct contact with powder or powder container.
* rapid deposition of energy at powder surface by high amplitude pulsed laser.
* impact of projectile against powder or container. This projectile can be accelerated by several means and velocities in the range of 200-3,000 m/s are required to produce the pressures listed in Figure 1. These projectiles can be accelerated electromagnetically, by compressed gases, by deflagration of gun powder, or by the detonation of explosives.

Of the different concepts introduced above, explosive compaction is the technique lending itself best to industrial production. Since the costs are low, the process lends itself to scale-up

without major problems. The effort by Raybould[10] at CERAC, a subsidiary of Atlas Copco, is noteworthy. Raybould developed a semi-automated machine capable of accelerating a piston at velocities up to 700 m/s. Parts could be repeatedly made with this assemblage with a diameter up to 7 cm. Net shape or near net shape was accomplished by the development of appropriate dies and momentum traps. In the following sections, explosive compaction systems used by the authors at New Mexico Institute of Mining and Technology will be described.

2.2 Cylindrical Configuration.

2.2.1 Single tube set-up.

This is the most common configuration used for shock compaction experiments. It is a very simple design and very little tooling is required around the material. Figure 3 shows the basic components of this system. The powder is placed in a metallic pipe with a diameter usually between 10 and 50 mm. End plugs are used to encapsulate the powder and the container is placed in a pipe (PVC, cardboard, steel). The pipe is filled with the chosen explosive and detonation is initiated at the top. The shock pressure on the powder can be varied by varying the amount and type of explosive. By increasing the detonation velocity from 3,500 m/s (the lowest range of ANFO--ammonium nitrate fuel oil) to 7,000 m/s (C-4 plastic explosive) the explosive pressure is quadrupled since the pressure varies with the square of the detonation velocity. The pressure pulse con-

verges towards the central axis of the cylinder and, if excessive, a hole is generated along the cylinder axis. This is called a Mach stem and can be eliminated by using a solid metal rod along the axis or by adjusting the shock and detonation conditions. This system lends itself well to the consolidations of powders that are fairly soft and ductile (hardness below 500 kg/mm^2).

2.2.2 Double tube set-up.

Considerable understanding of consolidation in the cylindrical geometry has been gained at New Mexico Tech, over the past seven years, during which a technique using the cylindrical geometry with two co-axial tubes was developed. The powder is contained in the internal tube. The external tube is surrounded by the explosive charge, which is detonated at one end; this external tube acts as the flyer tube, impacting the internal tube. This technique generates pressures in the powder that can be several times higher than the ones generated by the single tube technique. The main advantage of this technique is that it allows the use of low detonation-velocity explosives for consolidating hard powders. The lower detonation-velocity explosives minimize cracking of compacts. Significant improvements in compact quality have been obtained in nickel-base superalloys, titanium alloys and aluminum-lithium alloys.

The basic experimental set-up is shown in Figure 4. It is similar to the single-tube set-up. The explosive charge is detonated at the top; a Detasheet booster is used to create a

more uniform detonation front. The explosive is placed in the cylinder, at the center of which is the assembly containing the powder. The central axis of the container may have a solid rod, to eliminate Mach stem formation. The difference between the system shown in Figure 4 and the conventional explosive consolidation system, described in Section 2.2.1, is that a flyer tube is placed co-axially surrounding the container tube.

The radial cross-sectional view of the system employing the double tube configuration is shown in Figure 5. By applying an analysis similar to that developed by Gurney[11] for the velocity of fragments, one can estimate the velocity at which the flyer tube is accelerated inwards by the explosive. The chemical energy of the explosive is equated to the sum of the kinetic energy of the gases and that of the tube. One obtains the following equation:

$$V_p = \sqrt{2E}\ \{3/[5(m/c)+2(m/c)^2\frac{R+r_o}{r_o} + 2\frac{r_o}{R+r_i}]\}^{1/2} \qquad (5)$$

where V_p is the velocity of the flyer tube and m/c is the ratio between the mass of the flyer tube and the mass of the explosive charge. R and r_o are shown in Fig. 5. The importance of this equation is that it allows the selection of a pre-established pressure in the powder. The shock pressure is directly related to the impact velocity. Figure 6 shows the variation of the ratio $V_p/\sqrt{2E}$ with c/m. A more detailed description can be found in Meyers and Wang[9].

2.2.3 High-Temperature Set-Ups

When excessive cracking is present after room temperature shock consolidation, often improved results are obtained by pre-heating the powders. The high temperature can induce additional ductility to the powders and reduce their strength and hardness. Another advantage of high temperatures is that the shock energy required to melt the powder surfaces is decreased. Two systems developed at the CETR will be described here. The design of the high-temperature systems is such that the hot powder container is in close proximity to the explosive for a very short duration (usually, less then three minutes).

A schematic of the higher temperature test device is illustrated in Fig. 7. The heated powder container is dropped into a mild steel pipe (which acts as the flyer tube) by the release of a solenoid switch). The bottom portion of the mild steel flyer tube (equivalent to the height of the powder container) is surrounded by the explosive charge in a PVC pipe. The charge is initiated at the bottom using a detonator. Prior to the test, the powder container (loaded and sealed under argon atmosphere) is heated in a furnace at the desired temperature and loaded in the test device. Proper precautions are taken to minimize the temperature loss in the powder container by firing the charge in less than three minutes after the hot sample is removed from the furnace. The capsule is propelled upwards by the detonation at the bottom and has to be trapped. An armor plate standing on four support legs (Fig. 7) and having the bottom surface

protected by sand bags has been successfully used.

A more elaborate system, with enhanced safety features and in which detonation is initiated at the top, is shown in Figure 8. In this system, the hot capsule containing the powder is placed below the explosive charge. A push-tube activated by a counterweight raises the capsule until it penetrates the explosive charge (Figure 8(b)). The system is activated by a solenoid that releases the push-tube. In case of emergency or failure to detonate, a second safety solenoid drops the counter weight and the capsule is freed to drop from the explosive. This eliminates the possibility of accidental exposure of the explosive to high temperatures for prolonged times.

Both systems have been successfully used at CETR and have yielded good compacts of nickel-base superalloys and high temperature intermetallics.

2.3 Plate Configuration

The plate configuration is overall a preferred geometry, but sufficient information on it has not been accumulated by us. Our experience limits itself to a few experiments conducted on Al-Li-X alloys. Consolidation was successful but profuse cracking resulted. These partially unsuccessful results provided the guidelines for the design of the new fixtures. The key to designing fixtures while minimizing tooling (containers, anvils, etc.) lies in the use of balanced charges. The cylindrical

geometry owes its success to its design simplicity. One tube with two end plugs is practically all that is needed. The Al-Li-X plates used both an anvil and a bottom momentum trap (Fig. 9). Post-shock warping of the system is thought to have caused most of the cracking. This design did not use charge balancing. Fig. 9(b) shows the warping of the container and the cracking of the compact.

A proposed design that uses the same basic charge balancing concept as the cylindrical geometry is illustrated in Fig. 10, which shows the two juxtaposed rectangular containers in which the powder is placed. A solid metal anvil is placed between the two powder containers. The bottom portion of the containers has a momentum trap to capture the reflected waves. Fig. 11 shows the containers placed inside the explosive. Two flyer plates are symmetrically placed and will transmit the pressure pulse from the explosive to the powder container. Detonation is initiated at the top by a line wave generator (triangle with a hole pattern). Detonation propagates downwards, and the shock waves generated in the powder encounter each other in the central anvil, avoiding damage to the containers. This system can also be used without the flyer plates, when the pressure required is lower. In this case, the explosive will completely surround the capsule-anvil assembly. The system can also be adapted for high temperature shock consolidation, when it is necessary to preheat hard-to-compact powders so as to induce some ductility. Fig. 12 shows the modified system to be used. The powder containers will have thicker and wider anvils, so that they can be placed in the

system at a higher temperature. The containers will be heated in a furnace, then slipped above the explosive container (Fig. 12(a)) between the two guiding plates.

2.4 Sawaoka Shock Compaction Fixtures [12]

Very high pressure impact experiments can be conducted for consolidation of certain very hard and difficult-to-bond materials like ceramics. The Sawaoka fixtures utilize explosively driven plates for impact, to generate very high shock pressures (in the range of about 20-100 GPa[12]).

The set-up employs stainless steel flyer plates impacting stainless steel capsules at velocities of 1.5-3.0 km/s. The fixture configuration and the explosive assembly is shown in Figure 13. The flyer plate is accelerated downwards by the detonation of an explosive charge resting on its top. The explosive charge is initiated simultaneously over the top surface by an explosive system called "mousetrap assembly". It consists of a line-wave generator (perforated explosive triangle that initiates two layers of Detasheet C-2 placed on top of a glass). This is in essence the same set-up as that used in the early explosive shock recovery experiments for metals. Up to 8 or 12 individual capsules containing the powder can be utilized, and are held in cavities in the recovery fixture. A modified version of the Sawaoka set-up is shown in Figure 14. This employs acceleration of a flyer plate with a CETR-designed plane-wave lens. Impact planarity with this plane wave lens is better than

50 ns over 90% of the area of impact.

Numerical simulations of shock compression conditions in these recovery fixtures have been carried out with two-dimensional (CSQ) and three-dimensional (HULL) computer codes. For the impact of a stainless steel flyer plate on the stainless steel capsule at a velocity of 2.5 km/s, it has been found that two-dimensional effects within the low density powder samples dominate the loading process, and that interactions between the individual samples are negligible[13]. The analysis revealing the contours of maximum mean bulk pressure (in GPa) and temperature (in °C) in the sample cavity are shown in Fig. 15. The maximum pressure and temperature regions form at the corners and propagate toward the center and rear of the sample. In order to obtain a clear understanding of the process of shock compaction, it is very important to perform experiments with recovery fixtures that have been subjected to rigorous numerical simulation.

2.5 Sandia Calibrated Shock Recovery Fixture

The Sandia recovery fixtures for controlled shock loading and preservation of samples were developed with the intent of generating controlled and reproducible high pressure shock compression conditions. These fixtures allow a broad range of pressures and pulse durations. They were developed by Graham, Webb, and Davison[14-16] at Sandia National Laboratories. Table I shows the shock pressure and duration ranges achievable with

these fixtures. The Baby Bear capsule contains 1 cm^3 of powder; the Momma Bear capsule contains 5 cm^3 of powder; the Pappa Bear capsule contains 10 cm^3 of powder; the Bertha capsule contains 60 cm^3 of powder and the Big Bertha contains 100 cm^3 of powder. The copper capsule that contains the powder is surrounded by a 4340 steel block that provides containment support. The general arrangement of the explosive fixture is shown in Fig. 16. Copper is used for the capsule because it permits sealing of the sample cavity by plastic flow. Furthermore, optically flat surfaces required for intimate contact between the surfaces can be achieved with copper. Plane wave generators are used to initiate the explosive pads shown in Fig. 16. Here, unlike the Sawaoka compaction system, the explosive is in contact with the copper capsule and is not used to accelerate a flyer plate.

Two-dimensional computer simulations of the shock propagation process have also been conducted on these fixtures, and pressure and temperature histories are available. Thus, one can establish, after recovery and analysis of the shock modified material, the effects of pressure and temperature in a quantitative manner.

While the Graham fixtures are a superb research tool, they cannot be used to produce compacts because of their exceedingly high cost and because the compacts undergo considerable fragmentation due to tensile release waves. These fixtures should be used to establish the shock pressure and temperature necessary for good consolidation. With this knowledge in hand,

different fixtures (described in the preceding sections) should be used. Wang et al.[17] used the Bear series to independently vary the shock pressure and pulse duration and were able to determine the optimum consolidation conditions for the superalloy IN-100.

2.6 Convergent Wave Compaction Fixture (Yoshida Fixture[18])

This system employs the shock collision geometry to effectively increase the peak pressure, and is schematically illustrated in Fig. 17. The capsule is placed in the region where the shock waves coming from the right and left collide. The shock pressure experienced by the capsule is effectively twice the shock pressure in the single initiation systems. Thus, pressures in the megabar region are reached in the capsule and diamond consolidation (see Fig. 1) can be accomplished. Thermodynamic calculations show that the amplitude of the first shock wave going through the powder plays the most important role, and the following shock ringing and even the final peak pressure do not affect either the peak temperature and residual bulk temperature significantly for certain hard-to-consolidate powders. Such materials (e.g., diamond) have almost the same impedance as that of the surrounding stainless steel due to their high sound velocity. Hence, the pressure in diamond powder reaches the same level as steel when the first shock wave arrives at the downstream interface of powder and steel. Thus, unlike the system adopted by Sawaoka[12-13] and by Graham et al.[14-16], two-dimensional effects may not be too serious if the Yoshida

fixtures are employed for very high shock pressure compaction and synthesis of certain materials.

In this system, unlike the top detonation with a line wave generator described in Section 2.3 (for scale-up experiments in plate geometry), two plane wave lenses are used to initiate the explosive charges, which accelerate the flyer plates to impact the powder in the rectangular containers. The advantage of this system, apart from being able to generate very high pressures, is that the results of numerical simulation from small experiments can be directly extrapolated in scale-up for bigger plate dimensions. Furthermore, the Center for Explosives Technology Research has successfully developed plane-wave generating lenses, using a combination of emulsion and Detasheet explosives, which show dimensional stability giving a wave planarity of better than 50 ns over 90% of the lens face. Lenses of diameters of up to 12 inches have been used.

2.7 Computer Simulations

The key to scaled-up experiments, whether in cylindrical or plate geometry, is to obtain the correct state of shock pressures, temperatures and pulse durations witnessed in the powder, by using the proper two-dimensional computations. Computer simulations can provide a means to design experiments and to relate the distribution of material properties in the sample to stress history during consolidation. With this information the original experimental configuration can be redesigned.

There are several two-dimensional codes available, the most popular being the HEMP code developed by Wilkins[19] and its revised versions. This code solves the equations of continuum mechanics formulated in Lagrange coordinates, and is particularly suitable for computations in the cylindrical geometry involving a driver cylinder collapsing onto another cylinder containing the powder. An example of a calculation of the collapse of a steel cylinder onto a powder containing cylinder, performed using a revised version of the HEMP code, is shown in Fig. 18[20].

Extending the technique for fabricating cylinders to flat plates makes it possible to use similar computational calculations. Fig. 19 shows results of a computer simulation when the detonation front has just reached the steel end plugs at the bottom of the rectangular cans. The calculation, performed in two-dimensional plate geometry, is similar in appearance to that done with cylindrical symmetry. The rectangular containers placed back-to-back provide a plane of symmetry, and the container walls at the plane of symmetry serve as a mandrel. Placing a plate between the two cans (serving as an anvil), results in a more uniform stress distribution throughout the thickness of the powders. Computer calculations can also be used, on a more fundamental level, to predict the equations of state for the powders.

3. MATERIAL SYSTEMS

Shock-wave consolidation has several unique advantages over

conventional powder processing techniques. Bulk temperatures generated by shock consolidation are considerably below the recrystallization temperature for most materials. Hence, the metastable as well as fine homogeneous structures of the starting powders can be preserved after shock-processing. Another advantage of shock consolidation is that the resulting compact often undergoes shock-induced strengthening, which may result in improved mechanical properties. Furthermore, the dynamic consolidation technique can be used to shock synthesize novel phases and unique composites unattainable by conventional processing techniques.

In view of the above advantages, shock consolidation is particularly suitable for the processing of rapidly solidified metals, and very hard and difficult-to-bond ceramics. A variety of these metal and ceramic systems have been shock consolidated at the Center for Explosives Technology Research since 1983. These are listed in Tables II and III along with the nominal composition of the powder material, powder fabrication technique, particle size, and shock consolidation configuration. Figs. 20 and 21 show a series of micrographs illustrating the general morphology of typical rapidly solidified metal and ceramic powders. In general, the morphology of the metal powders is microcrystalline, microdendritic(Fig. 20f), or microcellular(Fig. 20d), characteristic of rapid solidification. The ceramic (diamond and c-BN) powders used were of different particle sizes, and were angular in shape. These were possibly sieved and refined through a crushing operation after synthesis.

Powders consolidated utilizing the cylindrical implosion configuration result in hollow or solid cylindrical rods up to 5 cm diameter and 50 cm long. Figure 22(a) shows titanium alloy cylinders of different sizes. The largest cylinder had a weight of 10 kg. Scale-up was not pursued beyond this point but is thought to be feasible up to 200 kg without significant problems or design changes. Fig. 22(b) shows a photograph of shock consolidated IN 718 Superalloy[21]. This cylindrical compact is fully densified (>98% T.D.) and is free of any macroflaws; however, if the alloys to be consolidated are brittle in nature then often times, the compact exhibits spiral cracking. This type of cracking was typically observed in the case of the TiAl alloy. An example of spiral cracking is shown in the macrophotograph of the longitudinal cross-section of a Ti-Al compact in Fig.23(a). Occasionally, transverse cracking, due to longitudinal tension generating along the length of the compact is also observed as shown in the macrograph in Fig. 23(b). Very often radial and circumferential cracks are observed along the cross-sections of cylinders (Fig.23(c) and (d)).

Small disks (1.2 cm dia. x 0.5 mm thick) of ceramic compacts (of diamond, c-BN) made by planar shock impact techniques have also been successfully recovered. Although these discs are better than 96% dense (shown in Fig. 24 (a)-(d)), radial waves generating due to the two-dimensional shock-wave loading conditions may create radial or circumferential cracks, as seen in the micrographs in Fig. 24(b) and (d). Furthermore, the

impact and the non-impact sides of the compacts exhibit different hardnesses and different degrees of bond strength, due to two dimensional loading conditions described earlier in Section 2.4.

4. MICROSTRUCTURAL CHARACTERISTICS

Shock-wave compaction is a very rapid densification process and does not involve prolonged thermal treatments. In this technique, consolidation of the powder to full solid density occurs by the passage of a shock wave of sufficient amplitude. Within a short time interval (rise time of shock wave ~50 ns [22]), the energy of the shock is utilized in plastically deforming or fracturing the powder particles, and reducing the void volume to virtually zero. This results in preferential heating of particle surfaces which can cause melting and inter-particle welding (in the case of metals), and melting and/or solid-state diffusional bonding (in the case of ceramics). The heating, melting, freezing, and bonding of particle surfaces occurs in time durations too small for atomic diffusion to occur over distances comparable to the particle size. Hence, the melted interparticle material rapidlysolidifies due to heat flow towards relatively cool particle interiors at rates as high as 10^5 - 10^{10} $^oC/s$, thereby retaining or even refining the initial RSP microstructure[22-29].

4.1 Shock consolidation mechanisms and microstructure evolution in metals

In general, the microstructure of the rapidly solidified powder compacted by shock consolidation is characterized by two regions:

a) the particle interiors, which remain unchanged, as revealed with optical microscopy observations. However, the deformation substructure observed by transmission electron microscopy is characteristic of shock hardened materials[30].

b) the interparticle regions, which exhibit severe plastic deformation and vestiges of interparticle melting and resolidification, confirmed by electron diffraction analysis.

Williamson and Berry[31] have performed calculations using a two-dimensional hydrocode that predict temperatures exceeding the melting point in the interparticle regions. Vreeland et al [22], based on a one-dimensional thermal analysis model, numerically computed melt temperatures, generating at interparticle regions in a glass forming Ni-based alloy. Confirmation of melting at interparticle regions in this material was obtained with electron microscopy observations[29].

Fig. 25 shows optical micrographs of six well consolidated alloys. Fig. 25(a) shows the microstructure of shock compacted MAR M-200 alloy[21]. The flow of material can be observed by the distortion of dendrites, especially near the boundaries of particles. The white poor-etching-contrast regions at inter-particle boundaries are due to melting and subsequent rapid solidification. Fig. 24(d) shows the superalloy IN 718[32]. The white-etching regions correspond to the material that melted and rapidly resolidified during the shock deformation process. The microstructure of the resolidified material is dictated by the cooling rate during the solidification process.

Fig. 25(c) is a micrograph of an Al-Li-Cu-Mg alloy compact. The smooth regions represent the original particles, while the curved "grainy" region is the molten pocket. In Fig. 25(b) optical micrograph of the titanium alloy Ti-17 is shown. Small white etching pockets, indicative of a melted and resolidified phase at interparticle regions (indicated by arrows), can be seen in the micrograph. Particle interiors on the other hand exhibit a contrast typically due to microcellular/microdendritic structure. Figs. 25(e) and (f) are optical micrographs of a Ti_3Al alloy compact. It is obvious that the particles have undergone extensive plastic deformation; however, the fine cellular structure in the particle interiors has been fully retained. Considerable jetting and extrusion at interparticle triple points is observed in micrograph 25(e), leading to localized melting at these regions (white etching regions). The metastable material thus produced has an extremely fine grain size (unresolved with an optical microscope), and therefore it yields a white etching contrast. In cases where the melt pools were of a larger size or were uniform around the particles, the melted material resolidified to an elongated cellular structure (grain size 1-5 μm), as shown in the micrograph in Fig. 25(f). The individual cells appear to have grown at solid particle surfaces and propagated towards the center of the melt pool leaving behind a trace of the solidification front. Often times the solidification of the melt is not complete and a shrinkage void results in the center of the melt pool. Figures 25(g) and (h) show these voids caused by solidification of melt pools in Ti_3Al and Mar M 200, respectively.

The TiAl alloy, in contrast to Ti_3Al, is very hard and brittle, and in spite of non-uniform melt formation at inter-particle regions (localized generally at particle boundary triple points), exhibits strong particle-to-particle bonding. Evidence of localized melting (material revealing poor etching contrast at interparticle regions) in this alloy is shown in the micrographs in Fig. 25(i) and (j). Due to the brittle nature of the TiAl alloy, the compacted material is unable to withstand any deformation as the consolidation front moves inwards during the shock implosion process (discussed earlier), resulting in cracks in the compact. However, most of the cracking observed in this material (Fig. 25(i,j)) is transparticle, indicating strong interparticle bonding.

In the process of shock consolidation, since the energy of the shock is inhomogeneously deposited at particle surfaces and within particle interiors, details of the general microstructure can only be confirmed with transmission electron microscopy. TEM observations made on a variety of compacts confirm that the structure of the molten pockets/areas (white non-etching areas at interparticle regions) is very different from that of the interior of the powder particles. Fig. 26(c) and (d) are a set of transmission electron micrographs near a white non-etching region in the IN 718 shock consolidated alloy (powder particle diameter 40 um), from a region shown in Fig. 26(b) (indicated by an arrow)[21]. The dendrites within the particle interiors appear to show extensive deformation as seen in the optical

micrograph TEM image in Fig. 26(a); whereas, the TEM image and selected area diffraction pattern in Fig. 26(c and d) correspond to an interparticle melted and resolidified region. The melt produced during the process of shock consolidation rapidly resolidified to a very fine grain size (<10nm) and dislocation-free structure. The diffraction pattern taken from this region (Fig. 26(c)) clearly shows that the reflections are from numerous individual grains.

A characteristic interface between the melted and resolidified particle surface and the unmelted particle interior is shown in the TEM image in Fig. 27 for the shock consolidated alloy[32]. The boundary is quite well defined, and there is no similarity between the features of the two adjacent regions. They can be seen separately in additional images and corresponding selected area diffraction patterns in Figs. 28(a) and (b). The almost continuous rings seen in the diffraction pattern in Fig. 28(b) are definite evidence of the extremely small size of grains produced during rapid solidification of the melt.

Similar results have also been obtained for titanium alloys (Fig. 29). Fig. 29(a) shows the interior of Ti-17 powder, consolidated by explosives. A well developed dislocation substructure can be seen in this bright field transmission electron micrograph. Fig. 29(b) shows a microcrystalline and dislocation-free grain structure, characteristic of the melted and resolidified interparticle region. Fig. 29(c) shows a micrograph

taken from a particle interior of a shock consolidated Ti-6242 alloy containing a uniform dispersion of erbia precipitates. These dispersoids are indicated by arrows, however, they cannot be seen clearly due to the presence of heavy deformation substructure. In order to reveal the erbia more clearly, and to demonstrate that the consolidation process did not significantly increase their size (< 50 nm), annealing treatment on the shock consolidated alloy was conducted followed by TEM observations. The substructure after two hours of annealing at 870^{o} is show in Fig. 29(d). The erbia dispersoids can clearly be seen and their size and spacing are such that they are effective high temperature strengtheners. Furthermore, grain growth in this material is also severely limited due to grain boundary pinning by the erbia precipitates.

4.2 Shock consolidation mechanisms and microstructure evolution in ceramics

The degree of densification of ceramic powders by shock consolidation is strongly dependent on the particle size of the starting material. It increases with increasing particle size and also with increasing shock impact pressure. Fig. 30 shows the dependence of relative density of shock compacted (a) diamond and (b) c-BN powders on the respective particle sizes. A lower degree of relative densification with the diamond powder (89% max) is observed, in contrast to c-BN (98%), which could be due to the effect of a large number of cracks in the recovered diamond powder compacts. In the case of the c-BN compacts which

are almost fully densified, x-ray diffraction results showed that a part of the fine (2-4 μm) c-BN powder was converted into turbostratic BN(t-BN) and graphite-like BN (g-BN) by the shock treatments. Thus the relative densities in Fig. 30(b) could contain some error, especially in compacts obtained from the fine 2-4 μm grade powder.

Ceramic powders can be densified and consolidated mainly by means of particle fracture and/or plastic deformation of particles under shock compression[33,34]. The former mechanism, particle fracture, usually results in a large particle size reduction in compacted powders, and the latter mechanism, plastic deformation, brings about a significant increase in lattice strain in the recovered materials[35].

Figs. 31(a) and (b) show the residual lattice strain and the crystallite size (based on x-ray diffraction line-broadening analysis) in the diamond powders compacted at 77, 90, and 108 GPa for different powder grades. At 77 GPa, the lattice strain values in the recovered diamond compacts are less than 0.05% and show no appreciable dependence on the initial particle size of the diamond. The reduction in particle size (calculated by crystallite size measurements) is also not appreciable in the diamond compacts made at 77 GPa. Hence, it appears that the 77 GPa shock pressure was not sufficiently high to induce extensive plastic deformation or fracture the particles, thereby resulting in little change in lattice strain and particle size.

With an increase in shock pressure to 90 GPa, the increase in lattice strain in the recovered diamond compacts shows a strong dependence on the initial particle size of diamond powder, as shown in Figs. 31(a) and (b). In the 2-4 um grade the lattice strain increases significantly to 0.18% and 0.23% for the top and bottom surfaces, respectively; while, the 0-1/2 μm grade powder also shows appreciable increase in lattice strain (at least on the bottom surface). As the particle size increases from 2-4 μm grade to 10-20 μm and 40-60 μm, the lattice strain gradually decreases. The lattice strain in the 10-20 μm grade diamond powder compacted at 90 GPa is only 0.1% and 0.2% on the top and bottom surfaces, respectively; where as in the 40-60 μm powder, the lattice strain drops to 0.09% (top surface) and 0.05% (bottom surface). The crystallite size analysis (figure 31(a) and (b), on the other hand, indicates that only the 10-20 um and 40-60 um grade powders show significant particle size reduction. This is also consistent with SEM observations of fracture surfaces of the compacts, shown in Fig. 32, which indicate that there is no significant particle size reduction in the 0-1/2 μm and 2-4 μm grade powders, while in the 10-20 μm grade and 40-60 μm grade powders, the particle size was reduced remarkably during shock compression.

From the residual lattice strain and particle size reduction found in the recovered diamond compacts, it is concluded that the 0-1/2 μm and 2-4 μm grade fine diamond powders are densified and consolidated primarily by plastic deformation of particles under shock compression at 90 GPa, while the 40-60 μm grade coarse

powder is consolidated mainly by particle fracture. The 10-20 μm powder can be consolidated by both the mechanisms, plastic deformation and particle fracture. At even higher pressures (108 GPa), similar consolidation mechanisms also apply; viz., consolidation via plastic deformation for fine powders and via particle fracture for coarse powders.

Shock consolidation of c-BN at 75 GPa, shows a relatively small increase of residual lattice strain in the recovered materials. The residual lattice strain and the crystallite size in the recovered 2-4 μm, 10-20 μm, and 40-60 μm grade c-BN compacts are listed in Table IV. Relatively small lattice strain values at least in the compacted coarse c-BN powders suggest that similar to the diamond powder compacts, coarse c-BN powders may be densified and consolidated by particle fracture, and the fine powders via the plastic deformation mechanism. However, scanning electron micrographs of the fracture surfaces of the compacts shown in Fig. 33, do not indicate significant changes in the particle size of the 40-60 μm powder compact. Therefore, it is reasonable to conclude that both the fine and coarse c-BN powders are consolidated by plastic deformation, rather than by particle fracture, and that the low lattice strain values in the recovered compacts are due to the annealing effects from the high temperature during shock compression. Also, the crystallite size of the compacted c-BN samples (listed in Table IV) is independent of the grain size of the starting c-BN powders. This suggests that heavily deformed c-BN particles are annealed and then recrystallized into 30-35 nm crystallites during shock compression.

5. MECHANICAL PROPERTIES

The mechanical properties of shock consolidated alloys are determined, in essence, by the bonding between the particles. If the bonding is perfect, the strength of the consolidated material should be equal to the strength of the material that constitutes the particles. However, bonding is not always observed to be of even quality. When the energy deposition at the particle surfaces is not sufficient for melting, the material is not densified, but the fracture surfaces follow the particle boundary path and the strength of the compact is very low. This is very well explained by the theory proposed by Schwarz et al[36], that predicts quantitatively a "consolidation" window. On the other hand, if substantial interparticle melting takes place, the fracture occurs through the particles.

Two contrasting cases are illustrated in Figs. 34(a), (b), (c) and (d). A fully densified (with perfect mechanical interlocking) titanium alloy (Ti-17), is shown in the scanning electron micrograph in Fig. 34(a). Fig. 34(b), on the other hand, shows a typical dimpled morphology of ductile failure, indicative of good consolidation (with perfect metallurgical bonding). The shock energy deposited in the latter case was sufficient for melting and resolidification, hence the fracture traverses the particles. The same fracture morphologies were observed for shock consolidated nickel-base superalloys. Figs. 34(c) and (d) show the interparticle and partial transparticle fracture modes, indicative of poor and good consolidation, respectively for

IN718. When the interparticle melting is not sufficient only mechanical interlocking between the particles takes place. Another example of transparticle failure in a shock consolidated TiAl intermetallic alloy, is also shown in Fig. 25(i,j).

Thus one concludes that the strength of the shock consolidated material should approach that of the shock-hardened alloy. Table V shows the strengths achieved in aluminum, titanium, and nickel-based superalloys. It approximates and in some cases exceeds, that of the conventionally processed (ingot-metallurgy) material. However, shock consolidation can only rarely be accomplished without flaws. In practice, it is the presence, size, and nature of the flaws (microcracks and micro-voids) that limits the strength of the shock consolidated material. Fig. 35 shows microcracks observed in shock-consolidated MAR M-200[37]. These microcracks are not visible at the lower magnifications used in Fig. 23 but they can have a profound effect on the strength of materials limited by flaw size. Fig. 35(a) shows a crack that nucleated at the inter-particle melting area where a void existed. Figs. 35(b) and (c) show cracks at more advanced stages of crack growth.

Recently, comparisons between shock consolidated materials with those processed by conventional powder metallurgy techniques have been conducted[38-40]. In the case of a nickel-based Pyromet 718 superalloy, shock consolidated using a propellant-fired gun at 1 km/s impact velocity, Thadhani et al[38], measured a yield strength of 1 GPa, which was at least 10% higher than

that of the hot isostatically pressed material. However, the shock consolidated material had practically zero ductility. Upon subsequent aging treatments (620°C for 8-40 hours), the yield strength and the ultimate tensile strengths were respectively 20% and 40% higher in the shock consolidated material in contrast to that processed by hot isostatic pressing, as shown in the plots in Figs. 36(a) and (b). Ductilities of the alloys processed by the two techniques were comparable following the aging treatment.

The superior tensile properties of the shock consolidated Pyromet 718 alloy were attributed to the fine grain size of the matrix, and an increased number of nucleation sites for the Ni_xNb precipitates, which lead to a larger number and finer size of the disk-shaped precipitation strengthening particles of γ". Fig 37 shows bright field transmission electron micrographs of γ" precipitates in (a) shock consolidated and (b) hot-isostatically-pressed Pyromet 718 alloy after 8 hours of thermal aging at 620°C. The nucleation of the γ" precipitates in the latter case is more sluggish, then that in the former. Hence, the density of γ" precipitates is considerably lower and they are at least two times the size of those in the shocked material, since no constraints are imposed during the growth of the precipitates in the case of the hot-isostatically-pressed material.

Flinn et al[39,40], compared the mechanical properties of explosively consolidated and hot-isostatically pressed (and cold worked) compacts of Fe-40Ni and Fe-40Ni-0.3NbC alloys, and AISI 304 Stainless steel powders. The mechanical properties for the

[39]

iron nickel alloys are listed in Table VI. The microhardness values for Fe-40Ni are comparable for the two consolidation methods; however, there appears to be a significant increase in the hardness for the explosively consolidated Fe-Ni alloy containing NbC, as a result of shock-hardening. The tensile property comparisons are contrary to those described above and observed by Thadhani et al[38]. The tensile properties of the explosively consolidated alloys, listed in Table VI, are poorer due to the particle bonding behavior, namely, localized yielding and plastic deformation at particle triple point regions. This results in melting and resolidification (and subsequent metallurgical bonding) only at these locally deformed regions, while the remaining particle perimeters are simply mechanically bonded, thereby resulting in poor bond strengths. The optical micrograph in Fig. 2, Ref. 39, clearly shows the bonding behavior in shock consolidated Fe-40Ni alloy.

Interparticle bonding behavior during shock consolidation is dependent on a number of factors, elucidated earlier in Section 2.1. The mode of shock loading used by the authors for the consolidation of these Fe-Ni alloys may lead to the localized deformation behavior, ~~as seen in Fig. 38(a).~~ Fig. 38, on the other hand, is an optical micrograph of a shock consolidated Pyromet 718 alloy[38]. The powder particles are bonded together by the interparticle regions which appear to have melted and rapidly solidified to a fine microcrystalline structure (non-etching regions). The almost uniform melt layer around particles is evidence of very strong bulk metallurgical bonding in this

material, and hence superior mechanical properties.

In many shock consolidated materials the ductility is considerably lower than that of conventionally processed materials. The reason for this lower ductility is probably connected with imperfect bonding between the particles or to the presence of voids and microcracks in the melted and resolidified regions. Fig. 39(a) shows the tensile strength of shock consolidated Ti-662 alloy as a function of temperature[41]. The ductility of shock-consolidated alloy at room temperature is approximately 0.04, compared with forged and aged material, with 0.10 ductility. Aging of the shock consolidated alloy improved the ductility slightly. Very worrisome is the decrease in ductility with increasing temperature for shock-compacted material, while the forged and aged alloy exhibited a significant increase in ductility. Hipping of the shock consolidated material significantly increased the ductility but caused a concomitant loss in strength. It is thought that hipping closes some of the microvoids and microcracks produced during shock consolidation. The use of shock-consolidation in association with conventional processing techniques has not been explored yet, but should be investigated in greater detail. Hot extrusion, hot rolling, and hot isostatic pressing are techniques that could be used in conjunction with shock consolidation to help to heal the microflaws produced by the latter process.

Shock consolidated ceramics, similar to metals, show significant increases in the hardness due to shock hardening.

The variation of microhardness with particle size for shock consolidated c-BN compacts is also superimposed in the plot in Fig. 30(b), which shows Vickers microhardness values increasing with increasing particle size. The average micro-hardness values in the front and rear surfaces of the 40-60 μm grade powder compact are 51.3 and 60.6 GPa, respectively, and are almost equivalent to those for statically synthesized poly-crystalline c-BN compacts[42]. This indicates that extensive interparticle bonding has been successfully produced in the coarse c-BN (40-60 μm grade) powder in the shock-compaction process.

The dependence of the microhardness of diamond compacts on the starting powder particle size is shown in Fig. 40. At 77 GPa mean shock pressure the microhardness values of the diamond compacts were very low (~10 GPa) and little dependence on the initial particle size was shown. As shock pressure increased from 77 to GPa, the microhardness values increased significantly, especially in the bottom surfaces of the compacts, and clearly showed large dependence on the diamond powder particle size. Maximum microhardness value of 84 GPa was obtained in the bottom surface (non-impact) surface of the 2-4 μm grade powder compacted at 90 GPa, which is equivalent to microhardness values reported in the static high pressure sintering of pure diamond powders [43]. The dependence of microhardness of diamond compacts on the initial particle size, which is different from that observed in the dynamic compaction of c-BN powders, appears to be closely related to the densification and consolidation mechanisms of diamond powders under shock compression. The large difference in

the microhardness values between the top and bottom surfaces of each diamond compact at 90 GPa is apparently due to the difference in the temperature history in both the regions during shock compression. This is a more distinguishing phenomenon in the diamond compact than in c-BN.

6. LIMITATIONS AND ECONOMIC FEASIBILITY

The two main limitations of shock consolidation are cracking and net shape capability. Cracking can be produced by tensile reflections, compressive stresses (shear instabilities leading to cracking) or by solidification shrinkage. Figs. 23, 24, and 25 show a variety of cracks in shock consolidated alloys and ceramics. While it is relatively simple to shock consolidate soft, ductile metals without cracking, the tendency for cracking increases as the ductility decreases. These cracks can be alleviated and possibly eliminated by design modifications; computer calculations can be very helpful in this matter. Smaller cracks, at the microstructural level, are also often observed (Fig. 35). These microcracks can have a very deleterious effect on mechanical properties, especially the low-cycle fatigue, which is one of the most important properties of nickel-based superalloys. RST alloys tend to be high-strength materials in which the load bearing ability is governed by the size of the cracks. Another source of flaws is shown in Fig. 35(a). The white-etching regions are molten and resolidified. Voids are formed in these regions. These voids are produced by solidification shrinkage. These voids can be nucleation sites for cracks. Fig. 25(g,h) shows similar features at a higher magnification.

Net shape capability will probably limit the production to simple shapes, such as cylinders, tubes, and plates. An exception might be small ceramic compacts for cutting tool

applications. The unavoidability of flaws in shock consolidated RST alloys will probably require further processing. Thus, shock consolidation should be combined with additional process, such as HIP, hot extrusion, rolling, or forging. Shock consolidation would be well suited as a component in a multi-stage process. The flaws present after shock consolidation could be healed in subsequent processing.

Scale-up has been attempted at New Mexico Institute of Mining and Technology and does not seem to present problems. Fig. 22(a) shows titanium alloy cylinders of increasing size. The scale in the figure is 12 in. long. The largest cylinder weighs 20 lbs and metallographic observation did not reveal any problems. The method described in Section 2 was used for the calculation of the scale-up parameters. Plans for the production of 200 lb cylinders are under way.

Although it is premature to make an economic feasibility study of the process at the present stage, a few preliminary calculations can be made. As an example, the production of a 200 lb titanium alloy billet (15 cm diameter and 200 cm long would require 500 lbs of explosive, at a cost of $75 ($0.15/lb). The tooling costs could be brought down to $500. Field set-up costs per shot could be as low as $400. This would result in a production cost of approximately $5/lb. The daily production of five 200 lb billets (~100 tons/year) could be carried out by a small company with a staff of 2-4 persons. This estimate does not include capital investment, depreciation, and administrative

marketing costs.

The production costs of small cutting tool bits would be considerably higher. At present, twelve 12 mm diameter disks of boron nitride or diamond can be compacted in one explosive event (see Sawaoka set up in Figs. 13 and 14). Eventually, systems could be developed in which as many as one hundred disks could be produced in one assembly. If we assure, to a first approximation, that machining costs are equal to $2,000, assembly and disassembly costs are equal to $1,500, and field set-up and firing costs are $500 we would have a cost of $40.00 per 12 mm disk. However, it is premature to develop economic analyses at the present stage, when significant technological barriers still exist before acceptable components can be produced. In terms of development efforts, what are needed are well established potential applications. Once these target products (in specified shape; with specified size and mechanical/microstructural performance requirements) are identified, the technological development can effectively take place, within the economic constraints. The direction of research effort has most often been the opposite in the past: novel materials have been shock consolidated into laboratory-sized samples that have been fully characterized with no specific intended application.

The authors hope that the overview presented in this chapter will stimulate industrial interest and activity in this field with specific objectives.

ACKNOWLEDGMENTS

The research described here was conducted in the period 1981-1988 with support from the National Science Foundation, General Electric, McDonnell Douglas, Center for Explosives Technology Research, Toshiba Tungaloy, and Pratt and Whitney. Graduate students involved in the work were S.L. Wang, L.H. Yu, H.L. Coker, S.N. Chang, D. Brasher, A. Ferreira, B.B. Gupta, and J. Kough. Other collaborators were Dr. T.C. Peng (MDRL), Dr. R. Graham (Sandia National Laboratories), Dr. A Szecket, and Mr J. Wessells and C. Austin (GE). The financial support and dedicated work of the collaborators is greatly appreciated. Special gratitude is extended to Mr. Dennis Hunter of TERA, Mr. Phil Anthony, and Mr. Thomas Gould of CETR, and to Drs. M. Brook and P.A. Persson for support and encouragement.

REFERENCES

1. O. Bergmann and N.F. Bailey, "Explosive Shock Synthesis of Diamond", in "High Pressure Explosive Processing of Ceramics", eds. R.A. Graham and A.B. Sawaoka, Trans Tech Publications, 1987, p.65.

2. S.Saito and A.B. Sawaoka, Proc. 7th Intl. AIRAPT Conference, High Pressure Science and Technology, Le Creusot, France, 1979, p.541.

3. N.V. Naumovich, Powder Metallurgy Association of Byelorussian Republic, Minsk, USSR, private communication, 1985.

4. A.A. Deribas, Special Design Office of High-Rate Hydrodynamics, Siberian Division of the USSR Academy of Sciences, Novosibirsk, USSR, private communication, 1985.

5. M. Cohen, B.H. Kear, and R. Mehrabian, "Rapid Solidification Processing - An Outlook," in Rapid Solidification Processing - Principles and Technologies (Part II), eds. M. Cohen, B.H. Kear, and R. Mehrabian, Claitor's Publishing Division, Baton Rouge, Louisiana, 1980.

6. W. H. Gourdin, Prog. in Materials Science, 30 (1986) 39.

7. "Dynamic Compaction of Metal and Ceramic Powders," NMAB-394, National Materials Advisory Board, National Academy of Sciences, Washington D. C., 1983.

8. L. E. Murr, K. P. Staudhammer, and M. A. Meyers, eds., Metallurgical Applications of Shock-Wave and High-Strain-Rate-Deformation, Marcel Dekker, New York, 1986.

9. M. A. Meyers and S. L. Wang, Acta Met., in press, 1988.

10. D. Raybould, in "Shock Waves and High-Strain-Rate Phenomena in Metals: Concepts and Applications," M. A. Meyers and L. E. Murr, eds., Plenum Press, New York, 1981, p. 895-911.

11. R. K. Gurney, "The Initial Velocities of Fragments from Bombs, Shells, and Grenades," BRL Report 405, 1943.

12. T. Akashi and A. Sawaoka, U. S. Patent 4,655,830; April 7, 1987.

13. F. R. Norwood, R. A. Graham, and A. Sawaoka, in "Shock Waves in Condensed Matter - 1985," ed., Y. M. Gupta, Plenum Press, 1986, p. 837.

14. R. A. Graham and D. M. Webb, in "Shock Waves in Condensed Matter - 1983," eds., J. R. Asay, R. A. Graham, and G. K. Straub, Elsevier Science Publishers, 1984, p. 211.

15. L. Davison, D. M. Webb, and R. A. Graham, in "Shock Waves in Condensed Matter - 1981," eds., W. J. Nellis, L. Seaman, and R. A. Graham, American Institute of Physics, New York, 1982, p. 67.

16. R. A. Graham and D. M. Webb, source cited in ref. 13, p.831.

17. S. L. Wang, M. A. Meyers, and R. A. Graham, "Shock Consolidation of IN-100 Nickel-Base Superalloy Powder," in "Shock Waves in Condensed Matter," ed., Y. M. Gupta, Plenum Press, New York, 1986, p. 731.

18. M. Yoshida, "Shock Consolidation of Pure Diamond Powders," CETR report, October, 1986.

19. M. L. Wilkins, "Calculation of Elastic-Plastic Flow," Report UCRL-7322, Lawrence Livermore National Laboratory, 1969.

20. M. L. Wilkins, A. S. Kusubov, and C. F. Cline, source cited in ref. 8, 1986, p. 57.

21. S.L. Wang, M.A. Meyers, and A. Szecket, J. Mater. Sci., in press (1988).

22. T. Vreeland, Jr., P. Kasiraj, A.H. Mutz, and N.N. Thadhani, in "Metallurgical Effects of Shock Waves and High-Strain-Rate Phenomena", eds. L.E. Murr, K.P. Staudhammer, and M.A. Meyers, Marcell Dekker, 1986, p.231.

23. D. Raybould, J. of Mater. Science,, 16 (1981) 16.

24. D. Raybould, Intl. J. of Powder Metal. and Powder Tech, 16, (1980) 9.

25. D.G. Morris, Metal Science, 16 (1982) 457.

26. D.G. Morris, Mater. Science and Eng., 57 (1983) 187.

27. W.G. Gourdin, J. Appl. Phys. 55 (1984) 172.

28. N.N. Thadhani, T. Vreeland Jr., T.J. Ahrens, J. of Mater. Science, 22 (1987) 4466.

29. N.N. Thadhani, A.H. Mutz, P. Kasiraj, source cited in Ref. 8, p. 247.

30. C.Y. Hsu, K.C. Hsu, L.E. Murr, and M.A. Meyers, in "Shock Waves and High-Strain-Rate Phenomena in Metals", eds. M.A. Meyers and L.E. Murr, Plenum Press, New York, 1981, Chap. 49, p.119.

31. R.L. Williamson and R.A. Berry, In "Shock Waves in Condensed Matter" APS Topical Conference-1985, ed. Y.M. Gupta, Plenum Press, New York, 1986, p. 341.

32. M.A. Meyers, B.B. Gupta, and L.E. Murr, J. of Metals, 33(10)(1981), 21.

33. T. Akashi and A. Sawaoka, J. of Mater. Science, 22, (1987), 1127.

34. T. Akashi and A. Sawaoka, J. of Mater. Science, V.22, 1987, p.1031.

35. T. Akashi, V. Lotrich, A. Sawaoka, and E.K Beachamp, J. Amer. Ceramic Soc., 68 (1985) c-322.

36. R.B. Schwarz, P. Kasiraj, T. Vreeland Jr., and T.J. Ahrens, Acta Met., 32 (1984) 1243.

37. M.A. Meyers and H.-r. Pak, J. of Mater. Sci., 20 (1985) 2133.

38. N.N. Thadhani, A.H. Mutz, and T. Vreeland Jr., submitted to Acta Met., Oct 1987.

39. J.E. Flinn, G.E. Korth and T.E. Doyle, in "Shock Waves in Condensed Matter-1987", eds. S.C. Schmidt and N.C. Holmes, North-Holland, 1988, p.415

40. J.E. Flinn, G.E. Korth and R.N. Wright, in Proc. of Intl. Conference on RSM, San Diego, ed. P. Lee, ASM, 1988.

41. M.A. Meyers, H.L. Coker, and N.N. Thadhani, "Shock Consolidation of Rapidly Solidified Titanium Alloy Powders", in Proc. of Intl. Conference on Rapidly Solidified Metals, San Diego, ed, P. Lee, ASM, 1988.

42. M. Wakatsuki, K. Ichinose, and T. Aoki, Mater. Res. Bull., 7 (1972) 999

43. H.D. Stromberg and D.R. Stephens, Ceram. Bull., 49 (1970) 103

LIST OF FIGURES

16. Section view of Sandia explosive compaction fixtures.

17. Schematic of experimental set-up employing the shock collision geometry for generating very high peak pressures (Yoshida fixture).

18. Calculation of the collapse of a steel cylinder onto a cylinder containg the powder to be compacted using the HEMP Code (from Wilkins et al. [20].

19. Calculated velocity vectors in ALN consolidated in plate geometry using the HEMP code (From Wilkins et al. [20].

20. General morphology of rapidly solidified metal powders; (a) MAR M-200, (b) Ti-17, (c) Al-Li-Cu, (d) section of Ti_3Al showing microcellular structure, (e) IN-718, (f) section of IN-718 showing microdendritic structure.

21. SEM of general morphology of ceramic powders (a) 10-20 um grade diamond powder, b) 40-60 um grade c-BN powder.

22. (a) Shock consolidated Ti-alloy cylinders of different sizes.
(b) Shock consolidated IN 718 superalloy hollow cylinder.

23. Macrophotographs of longitudinal sections of shock consolidated Ti-Al alloy showing (a) spiral and (b) transversal cracking. Additional cracks often observed in shock-consolidated cylinders: (c) radial cracks, (d) circumferential cracks.

24. Section views of typical top (impact) and bottom (non-impact) surfaces of shock consolidated (a)-(b) diamond powder and (c)-(d) c-BN powder compact.

25. Optical micrographs of well consolidated alloys (a) MAR M-200, (b) IN 718, (c) Al-Li-Cu, (d) Ti-17, (e) Ti_3Al, (f) TiAl; Flaws in well consolidated alloys, (g)-(h) solidification voids in the Ti_3Al and Mar M 200, respectively, (i)-(j) transparticle cracks in TiAl.

26. Transmission electron micrographs showing interparticle melting region in superalloy IN 718,
(a) optical micrograph showing perforation, white interparticle regions, and region observed in transmission electron microscope
(b) higher magnification of (a) in TEM
(c) diffraction pattern showing microcrystalline structure
(d) transmission electron micrograph showing microcrystals with diameters of 20-50 nm.

27. TEM image showing interface between melted and resolidified particle surface and unmelted particle interior in MAR M-200(from [32]).

28. (a) TEM image showing extensively deformed particle interior, and (b) TEM image and SAD pattern showing evidence of melted and resolidified interparticle region (from [32])

29. Transmission electron micrographs of shock consolidated titanium alloys; (a) well-developed dislocation substructure in Ti-17 particle interior (b) interparticle melting region having microcrystalline and dislocation-free grains in Ti-17 alloy, (c) Erbia dispersion after onsolidation in Ti-6242 + Er alloy, (d) uniform erbia dispersion in shock consolidated and aged Ti-6242+ Er alloy.

30. Dependence of relative density of shock compacted (a) diamond, and (b) c-BN powders on the respective particle sizes.

31. Residual lattice strain and crystallite size in shock compacted (a) 0-0.5 μm and 2-4 μm grade; and (b) 10-20 μm and 40-60 μm grade diamond powder.

32. SEM photographs of fracture surfaces near the central region of the bottom (non-impact) surfaces of (a) 0-1/2 μm, (b) 2-4 μm, (c) 10-20 μm, and (d) 40-60 μm grade powders, compacted at 90 GPa.

33. SEM micrographs of fracture surfaces of top and bottom regions of compaced c-BN powders. (a)-(b) 2-4 μm grade and (c)-(d) 10-20 μm grade, (e)-(f) 50-60 μm grade.

34. Scanning electron micrographs of (a) poorly bonded, (b) well bonded Ti-17 alloy, (c) poorly bonded IN 718, (d) well bonded IN-718.

35. Fracture nucleation in MAR M-200 superalloy
    (a) Fracture initiation at void formed in interparticle melt region
    (b) microcracks between grains
    (c) intergranular cracks.

36. Tensile property comparison between shock consolidated and hot-isostatically-pressed Pyromet 718 alloy: (a) Yield strength versus aging time and (b) ultimate tensile strength versus aging time.

37. Bright field transmission electron micrographs of γ'' precipitates in (a) shock consolidated and (b) hot isostatically pressed Pyromet 718 alloy after shows of aging of 620°C.

38. Optical micrograph of shock consolidated ~~(a) Fe-40 Ni and~~ nickel-based Pyromet alloy powder showing interparticle bonding behavior.

39. Variation of (a) yield stress and (b) total elongation with

temperature for Ti-662 in shock-consolidated, shock consolidated + aged (570°C/4 hours), shock consolidated + hipped conditions; forged + aged (570°C/ 4 hours) matrial given for comparison.

40. Dependence of microhardness of diamond compacts on the starting powder particle size.

LIST OF TABLES

TABLE I
BASIC CHARACTERISTICS OF SANDIA SHOCK RECOVERY FIXTURES

Fixture	Explosive	Pressure GPa Range	Avg	Duration μs
Bertha	B	3 - 4.5	4	11.2
Papa Bear	B	3.6- 6.0	5	6.4
Big Bertha A	B	4.6- 7.5	6	15
Bertha A	B	5 -10	7.5	11.2
Momma Bear	B	5 -10	7.5	4.5
Papa Bear	C	6.5- 9.5	8	6.4
Big Bertha A	C	10 -16	13	15
Momma Bear A	B	14 -20	16	4.5
Bertha A	C	14 -26	17	9.8
Baby Bear	B	13 -26	20	2.5
Momma Bear A	C	19 -26	22	4.7
Baby Bear	C	22 -32	27	2.6

TABLE - II POWDER CHARACTERISTICS AND COMPACTION APPROACH FOR METALS

POWDER TYPE	NOMINAL COMP. (wt%)	POWDER FABR. TECHNIQUE	PARTICLE SIZE	SHOCK CONSOL. CONFIGURATION
MAR M-200		rapid solid. rate process	37-74 μm	cylindrical - single tube
IN 100				cylindrical - single tube
IN 718				cylindrical - single tube
Ti-17	5Al,2Sn,2Zr,4Mo 4Cr,bal Ti	rotating electrode process	50-250 μm	cylind. single & double tube
Ti-662	6Al,2Sn,6V,1Tl, 1Cu, bal. Ti	plasma rotating electrode process	50-250 μm	cylindrical - single & double tube
Ti-6242	6Al,2Sn,4Zr,2Mo 1Er, bal. Ti	rapid solid. rate process	50-250 μm	cylindrical - single & double
Al-Li-Cu	Al, Li, Cu, Mg, Zr			cylind. single /double tube & planar plate impact
Al-Fe-Ce	Al, Fe, Ce,			cylind. single /double tube & planar plate impact
TiAl	34 Al, 1.3 V balance Ti	rotating electrode process	50 to -200 mesh	cylind. double tube and plate impact (balance charge) at room and high temp.
Ti_3Al	14 Al, 21 Cb balance Ti	rotating electrode process	-80 mesh	cylind. double tube and plate impact (balance charge) at room and high temp.

TABLE-III POWDER CHARACTERISTICS AND COMPACTION APPROACH FOR CERAMICS

POWDER TYPE	NOMINAL COMP. (wt%)	POWDER FABR. TECHNIQUE	PARTICLE SIZE	SHOCK CONSOL. CONFIGURATION
Diamond*	commer. powder with following ppm impurities: 800Si,10Mg,10Mn Ni,Cu,Ca < 5 Al,Fe,Cr <1	General Electric synthetic grade	0-1/2, 2-4, 10-20, 40-60 microns	12-capsule plate impact Sawaoka fixture
Diamond**	natural and synthetic powd.	DuPont and GE synthetic grades	0-1/2,1/2-1 5-7, 50-60 microns	Convergent wave compaction fixture
cubic-BN*	commer. grade powder with the following ppm impurities: 800Si,100Mg,5Ca 10Mn, Fe,Cr <1	Showa Denko Co. Ltd. Japan General Electric synthetic grades	2-4 um 10-20 um 40-60 um	12-capsule plate impact Sawaoka fixture

*Work performed by A. Sawaoka (Tokyo Institute of Technology) and T. Akashi (Toshiba Tungalloy), and **Yoshida, at the Center for Explosives Technology Research, New Mexico Tech.

TABLE IV
LATTICE STRAIN AND CRYSTALLITE SIZE
OF SHOCK COMPACTED c-BN POWDERS

Grain Size	Lattice Strain (%)		Crystallite Size (nm)	
	Top	Bottom	Top	Bottom
2- 4 um grade	0.29	0.26	36	32
10-20 um grade	0.19	0.19	30	33
40-60 um grade	0.17	0.14	31	31

TABLE V
TENSILE PROPERTIES OF SHOCK CONSOLIDATED
RAPIDLY SOLIDIFIED ALLOYS

Material	Y.S. (MPa)	T.S. (MPa)	RA%
* Al-3Li-1Cu-1Mg-0.2Zr		282	
* Al-8.4Fe-7Ce		256	
* Al-3Li-1Cu-0.2Zr		265	
** Ti-17	1,215	1,233	5
** Ti-662	1,118	1,166	2.5
IN 718 (RT cons.)	534	761	
IN 718 (cons. at 525°C)	877	1,165	
IN 718 (cons. at 740°C)	540	787	
IN 718 (cons. at 740°C + aging)	901	1,239	
MAR M 200			

* Tests performed by McDonnell Douglas Research Laboratory
** Tests performed by GE

TABLE VI
MECHANICAL PROPERTIES OF EXPLOSIVELY AND HIP + 50% COLD ROLLED CONSOLIDATED FE-40NI POWDERS [39]

Specimen	Consolidation Condition	Hardness[a] DPH	0.2% Offset Yield, MPa	Ultimate, MPa	Total Elong. %	Reduction in Area, %
CA Fe-40Ni	Dynamic	209 ± 11	513	634	4.6	1.2
CA Fe-40Ni	HIP + CW	222 $^{+2}_{-5}$	678	690	18	55
VGA Fe-40Ni	Dynamic	214 $^{+8}_{-12}$	536	632	4.7	2.8
VGA Fe-40Ni	HIP + CW	217 $^{+5}_{-3}$	621	655	18	53
CA Fe-40Ni-0.3 NbC	Dynamic	260 $^{+4}_{-7}$	512	679	4.7	0.5
CA Fe-40Ni-0.3 NbC	HIP + CW	228 $^{+7}_{-8}$	707	722	19	57
VGA Fe-40Ni-0.3 NbC	Dynamic	254 ± 4	547	686	4.3	2.0
VGA Fe-40Ni-0.3 NbC	HIP + CW	232 $^{+11}_{-10}$	679	717	23	59

a. ± represents upper and lower increments observed from the numerical average.

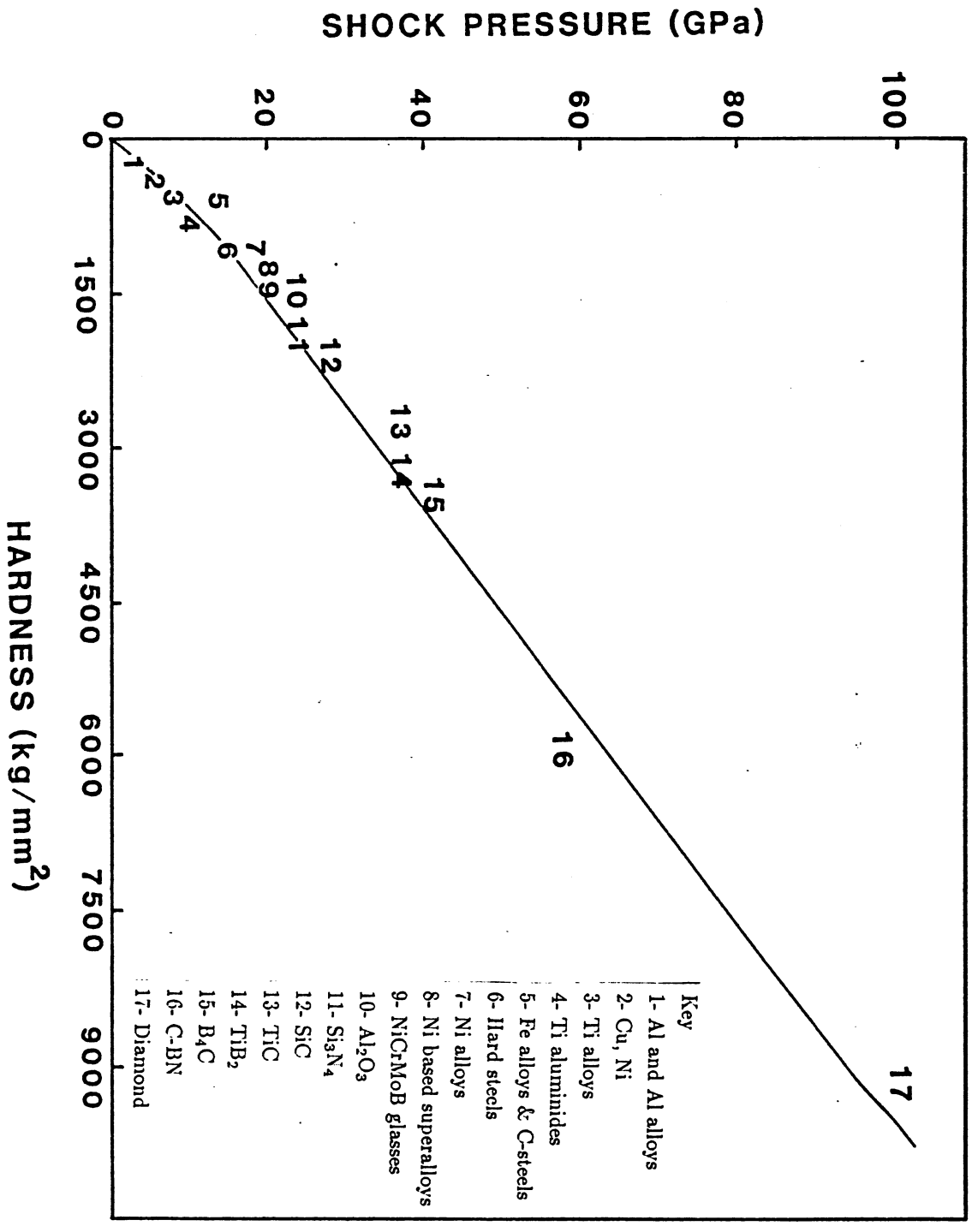

1. "Engineering" correlation between powder hardness and pressure required for shock consolidation.

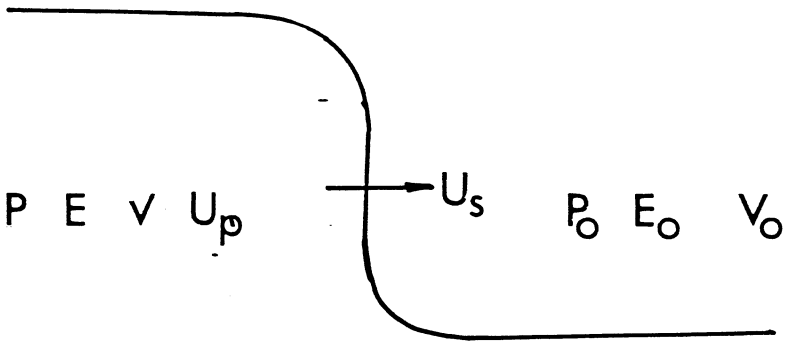

(a)

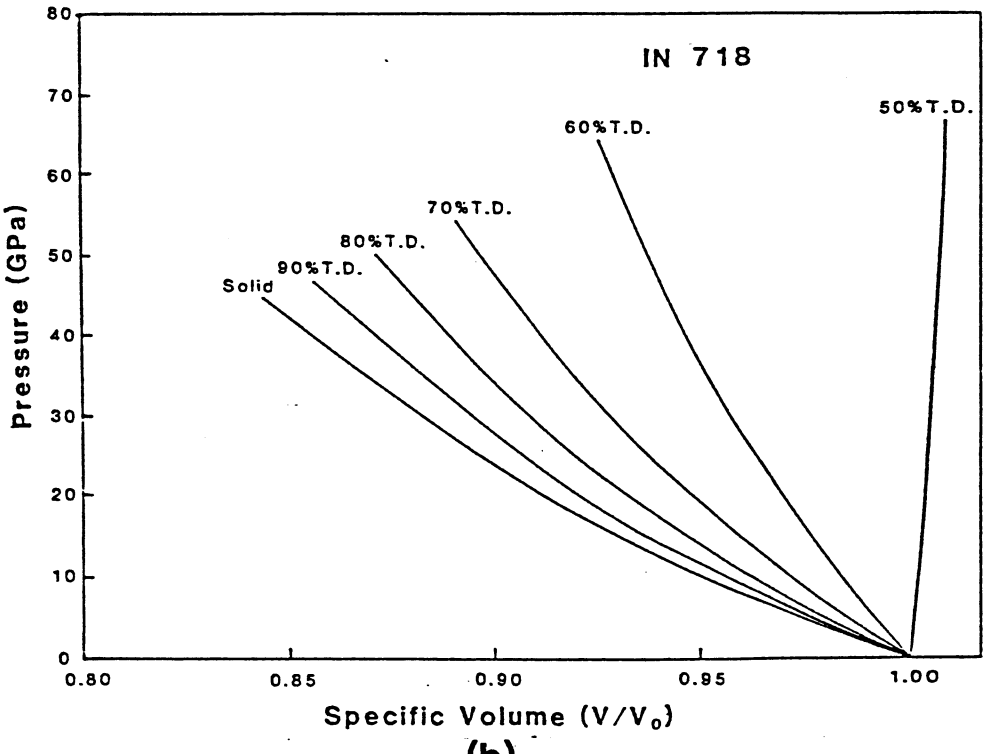

(b)

2. (a) Schematic of shock wave propagation.
(b) Pressure-specific volume curves generated for INCONEL 718 powder at different initial porosites.

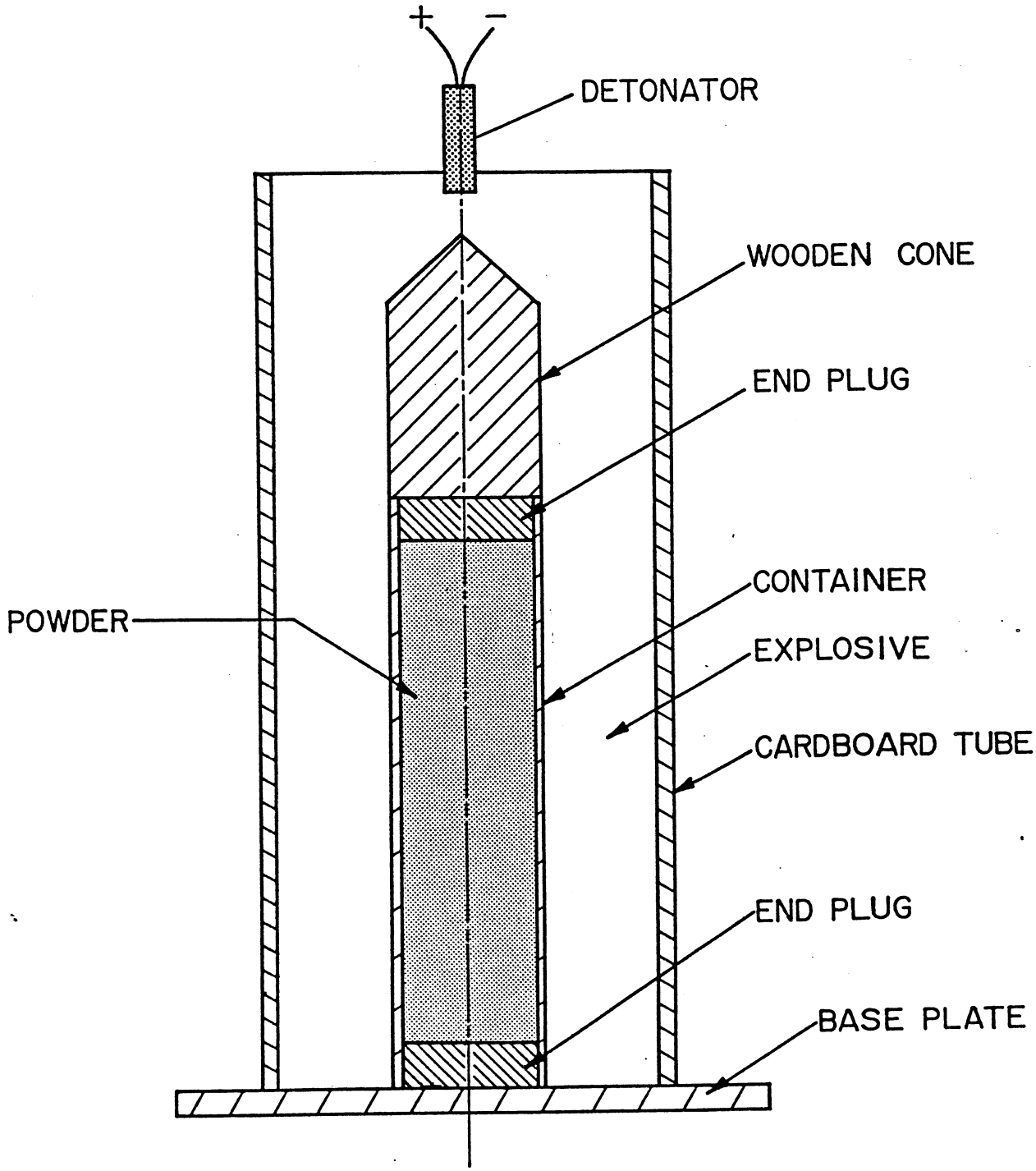

3. Basic components of a simple cylindrical compaction system.

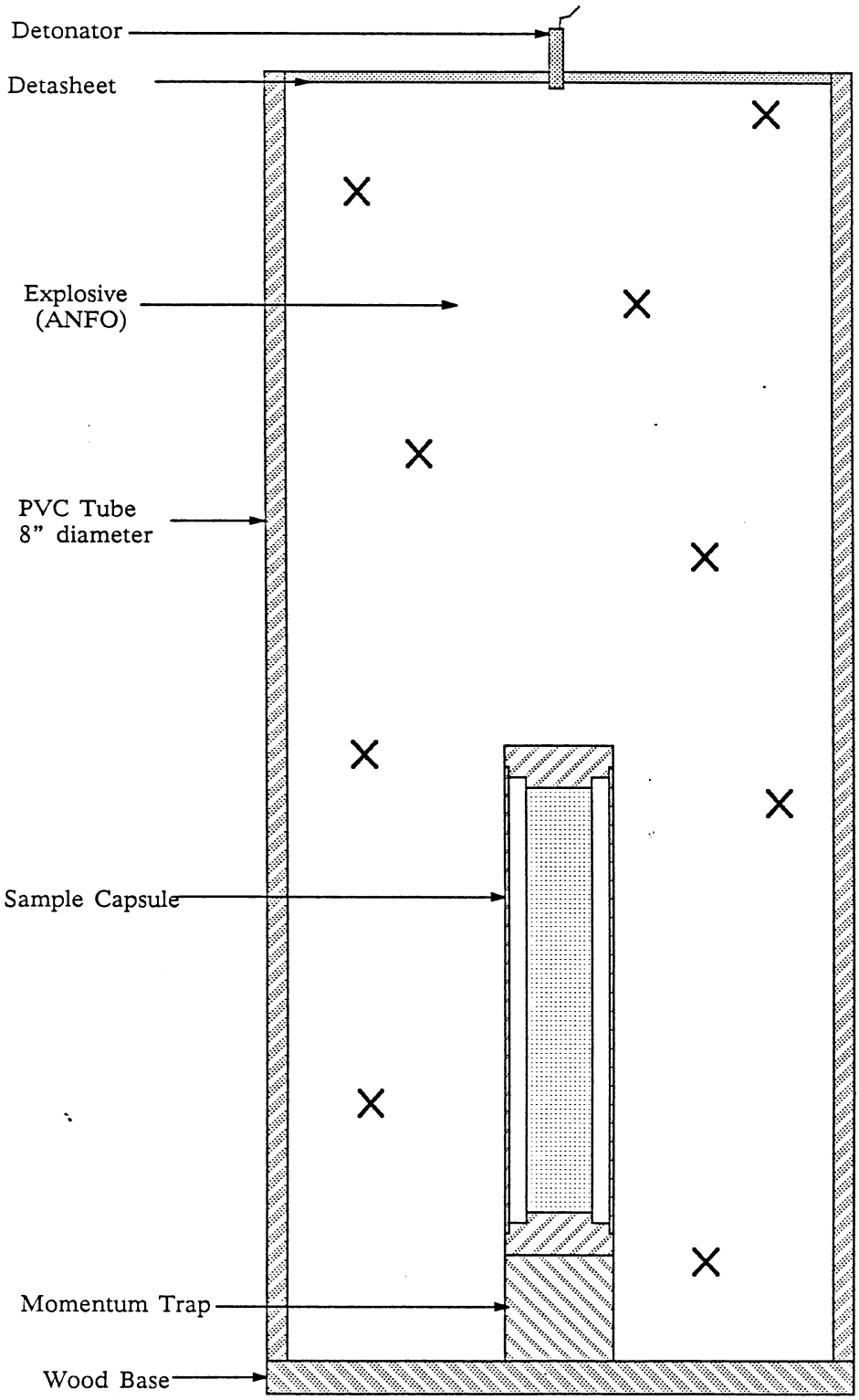

4. Basic experimental set-up for the cylindrical axismmetric double tube system.

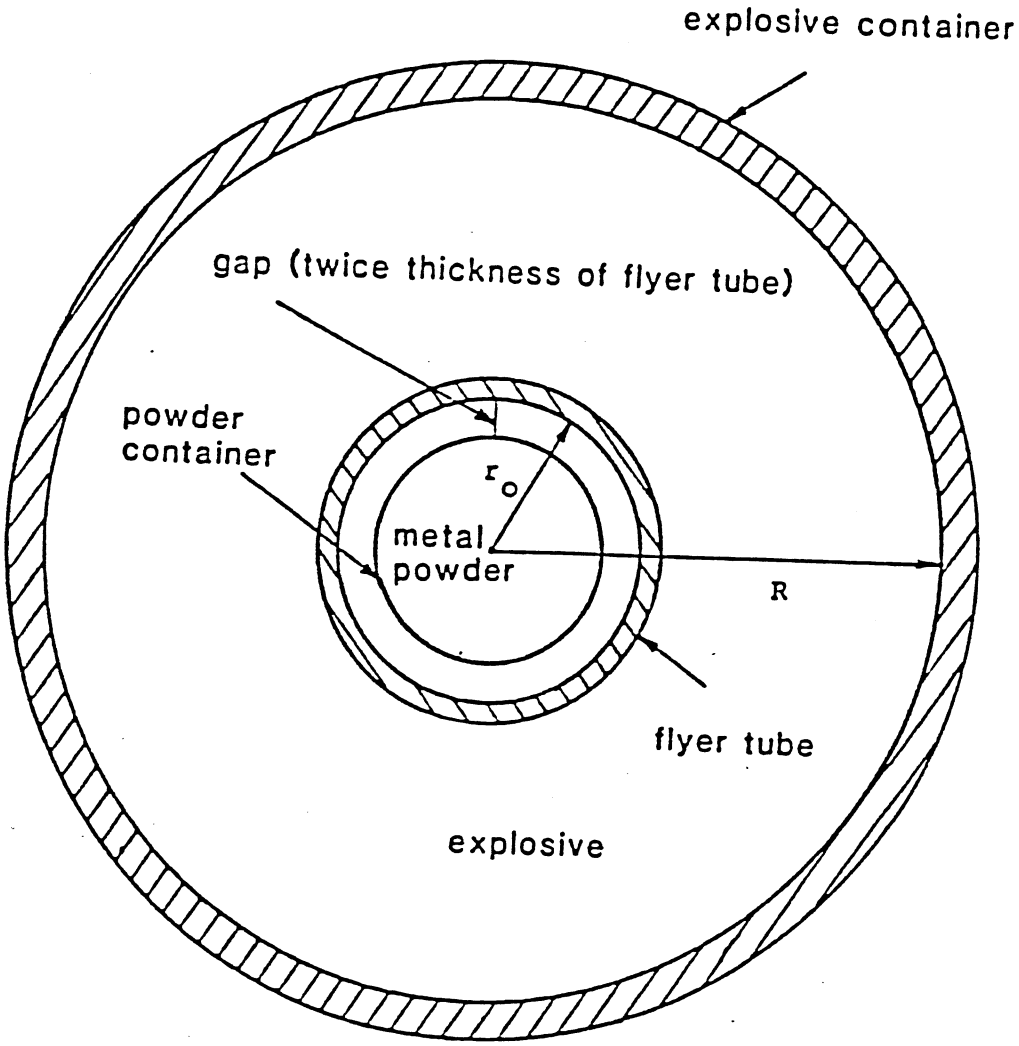

5. Radial cross-section view of system employing the double-tube configuration.

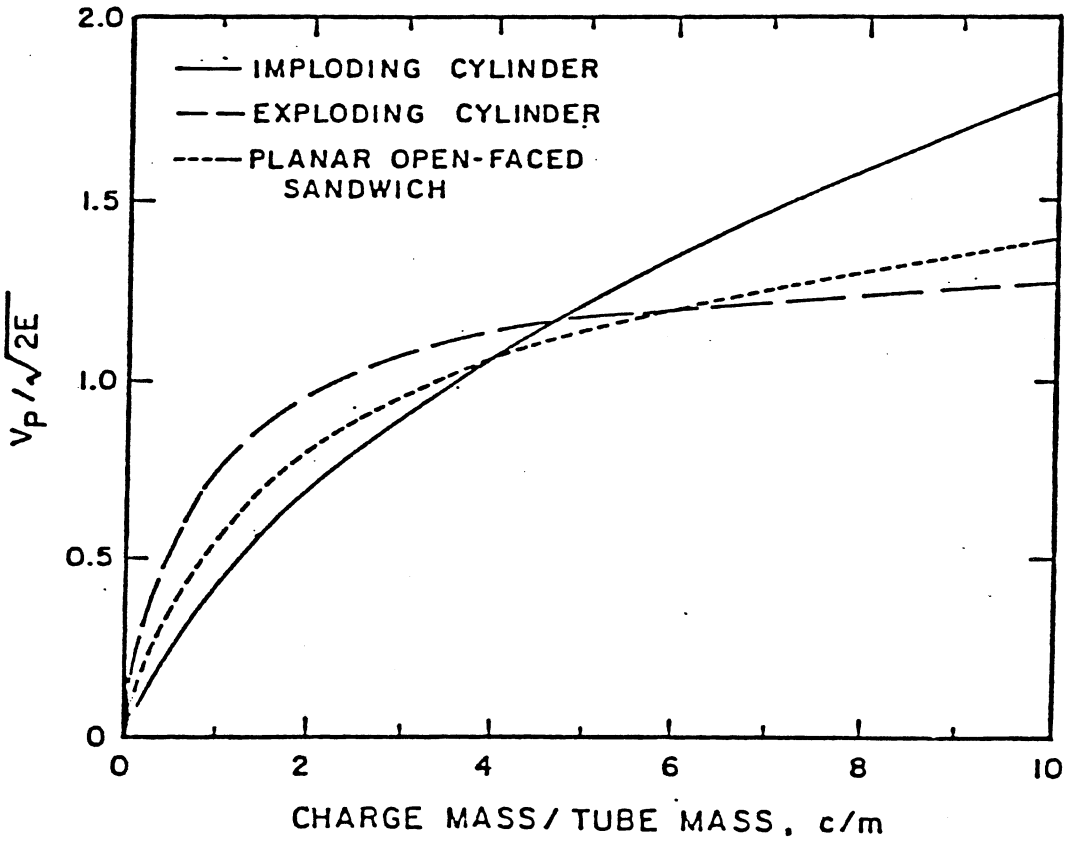

6. Dimensionless velocity of metal as a function of loading factor c/m for various geometries.

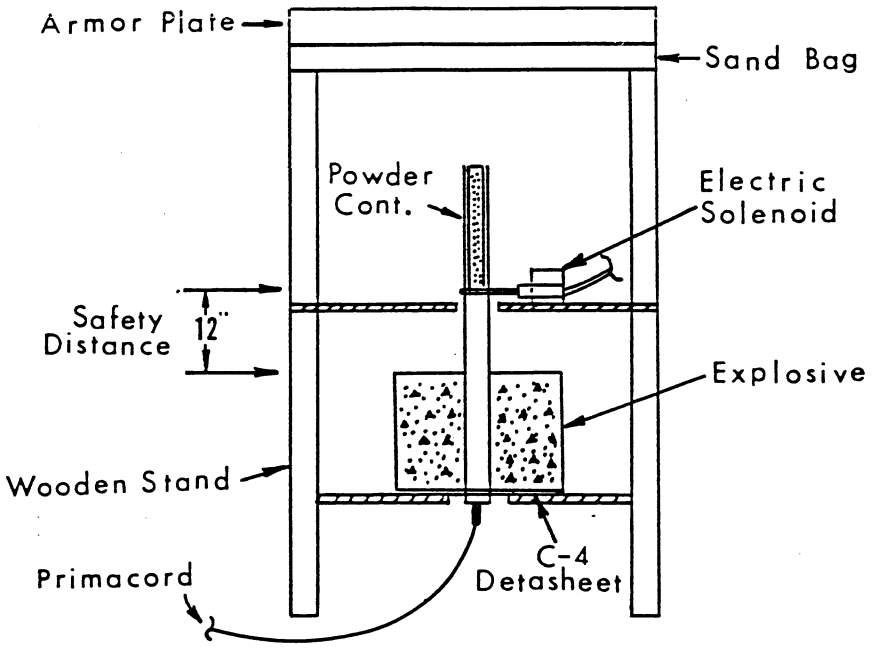

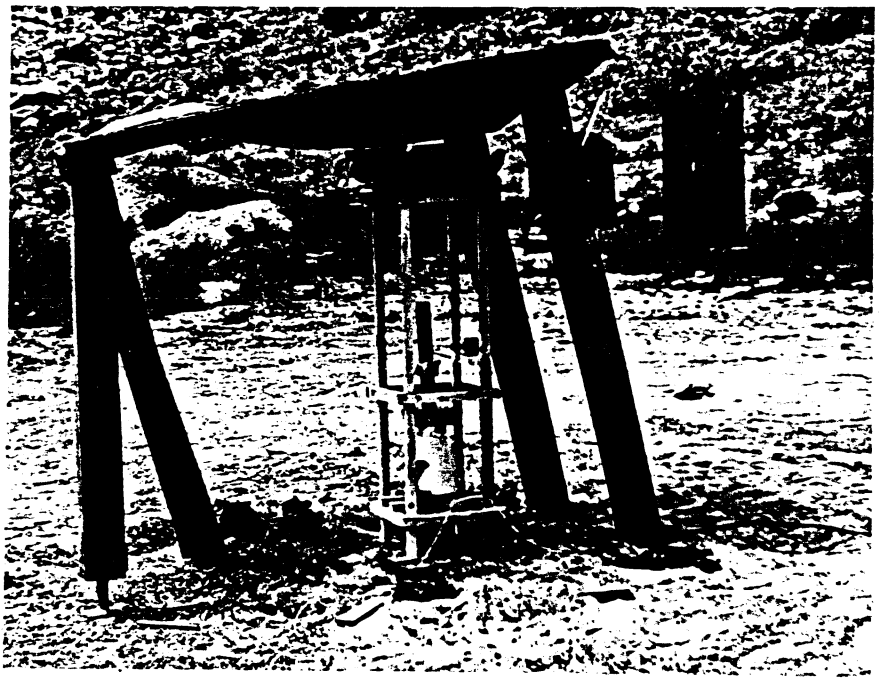

7. High temperature test device employing the double-tube technique for compacting powders pre-heated above ambient temperature.

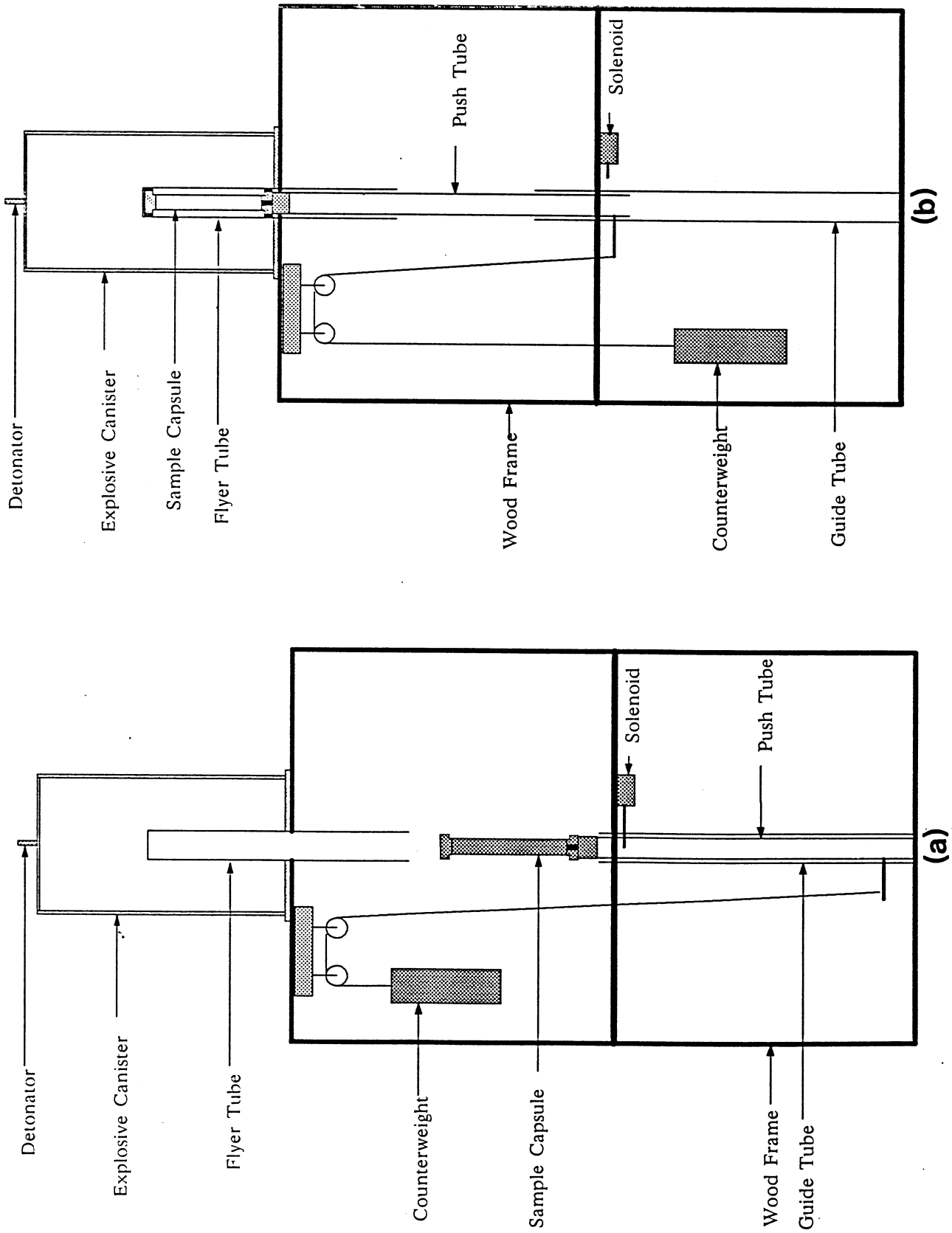

8. Schematic of high temperature test device (with enhanced safety features) in which detonation is initiated at the top.
   (a) powder container ready for insertion.
   (b) powder container in explosive charge.

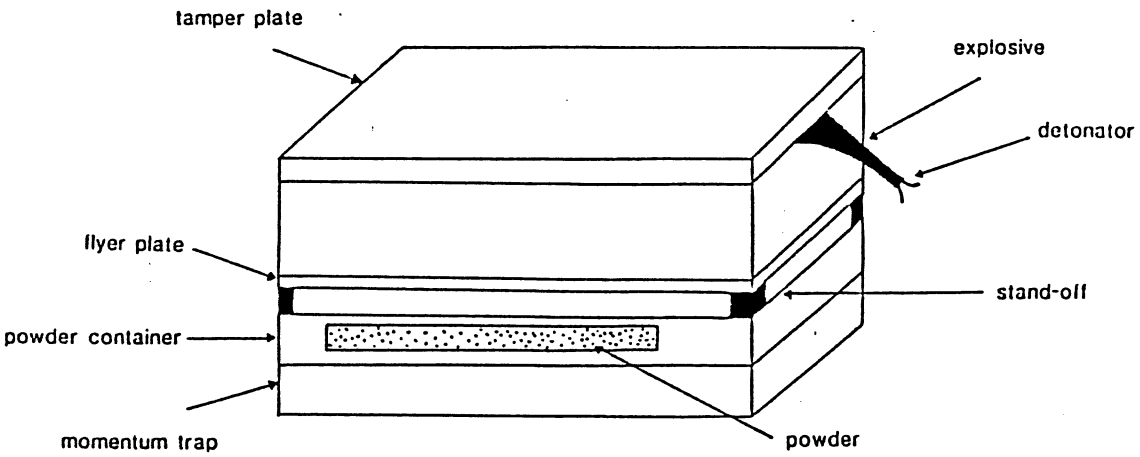

(a)

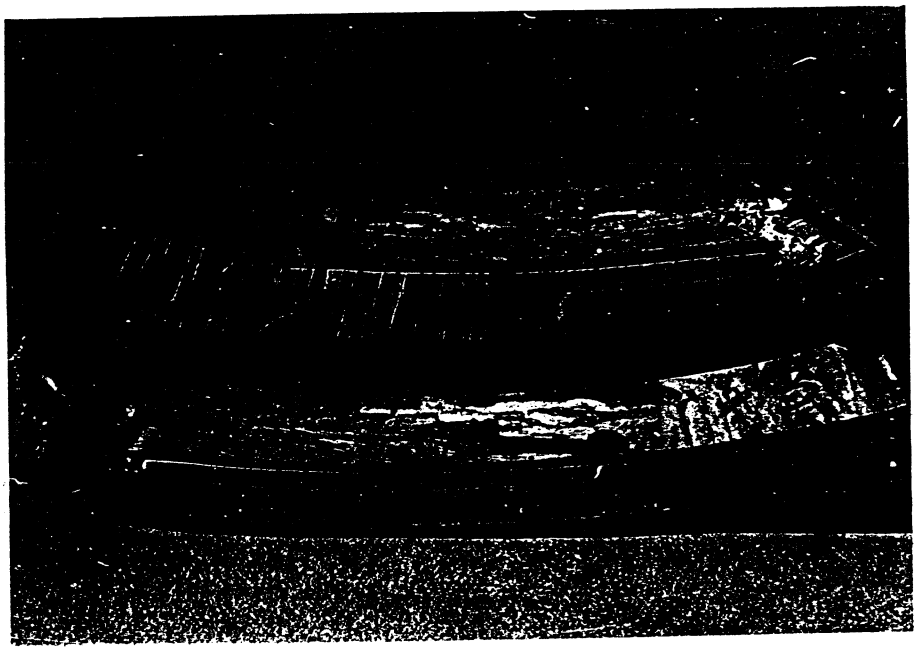

(b)

9. (a) Set-up for consolidating Al-Li-X alloys employing an anvil and a bottom momentum trap.
(b) Photograph showing warping of the container and cracking of the compact made with system shown in (a).

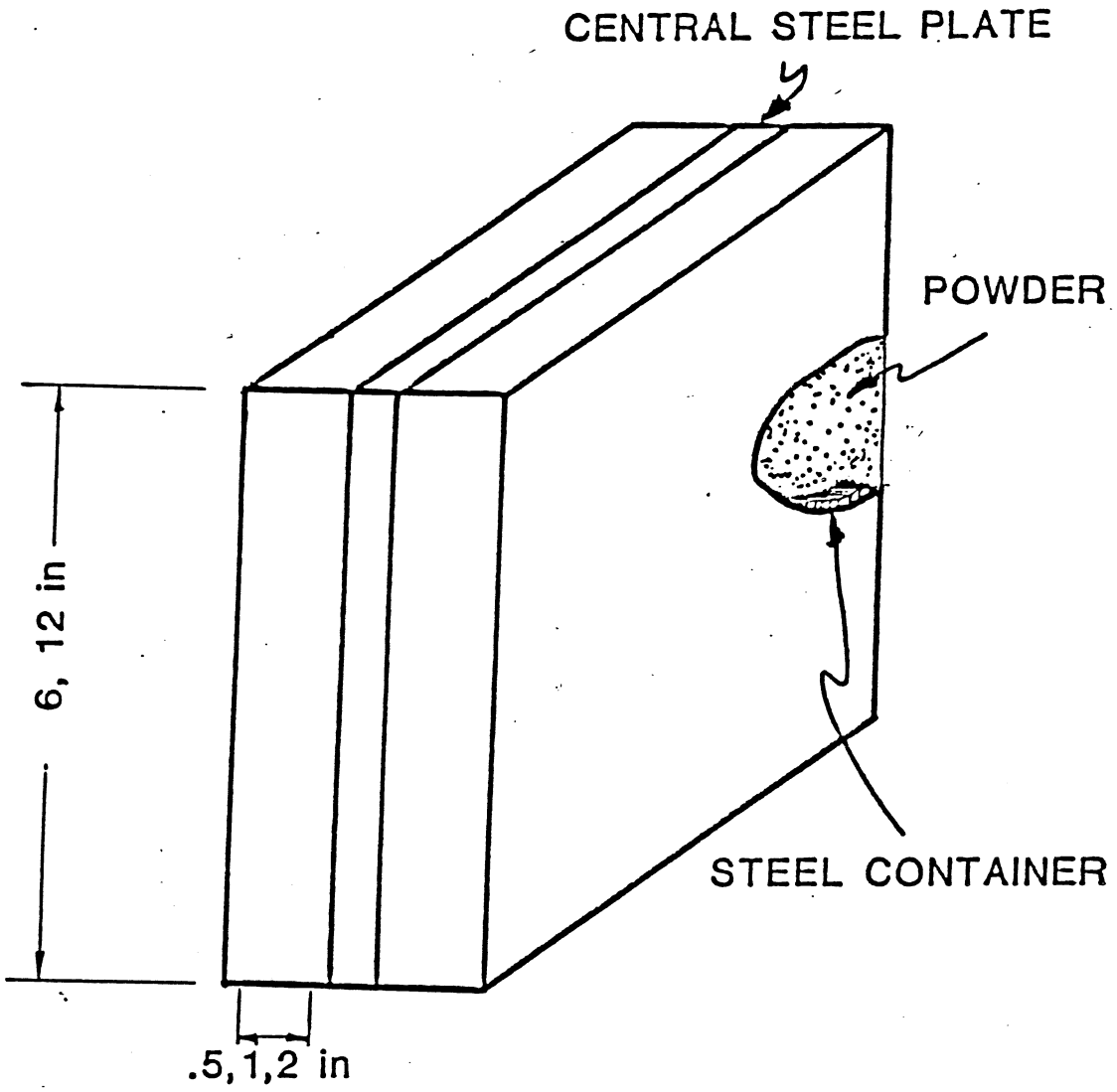

10. Containers for the consolidation of plates, using the charge balancing concept.

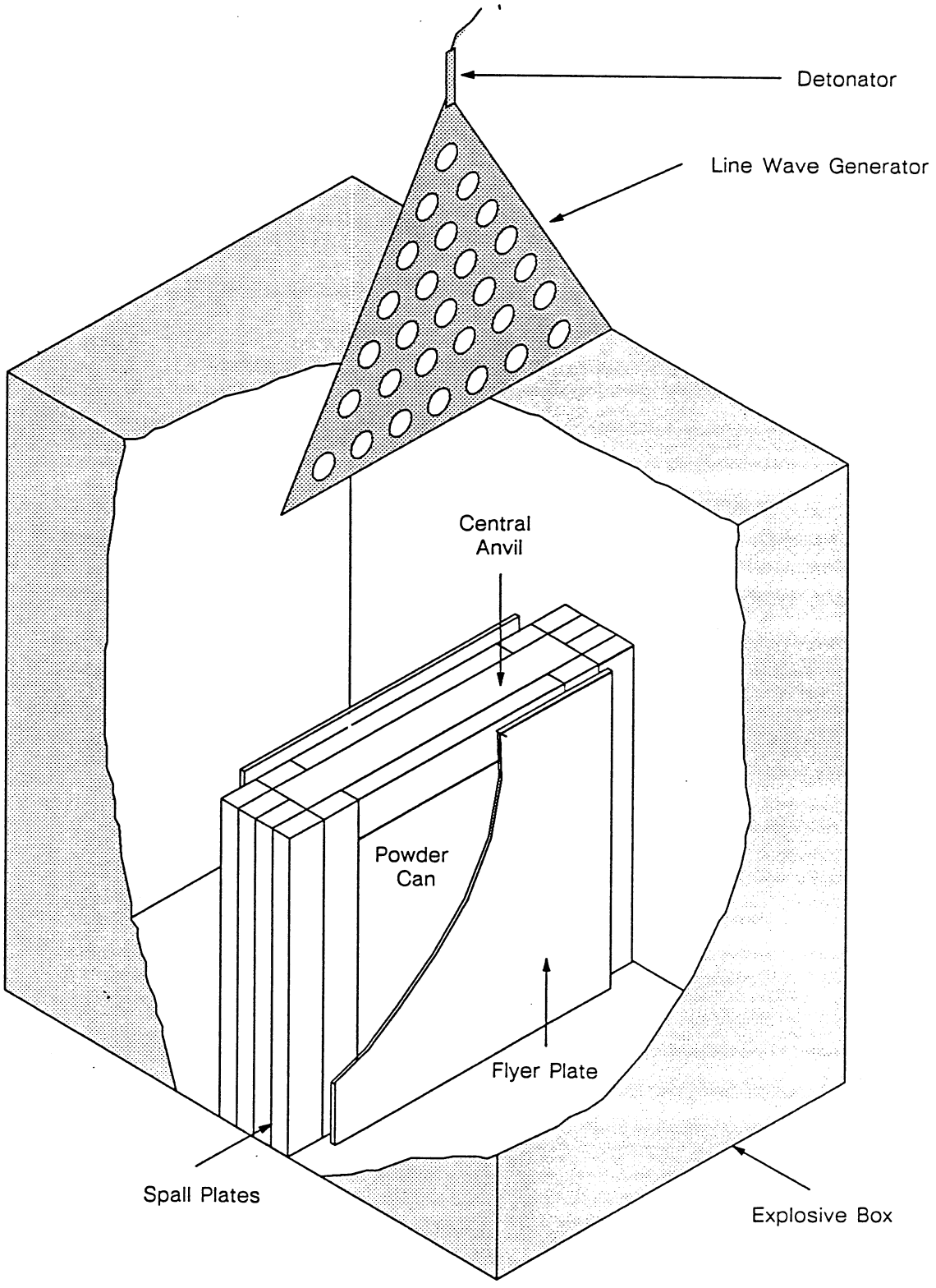

11. Schematic of the plate configuration set-up employing the charge balancing concept.

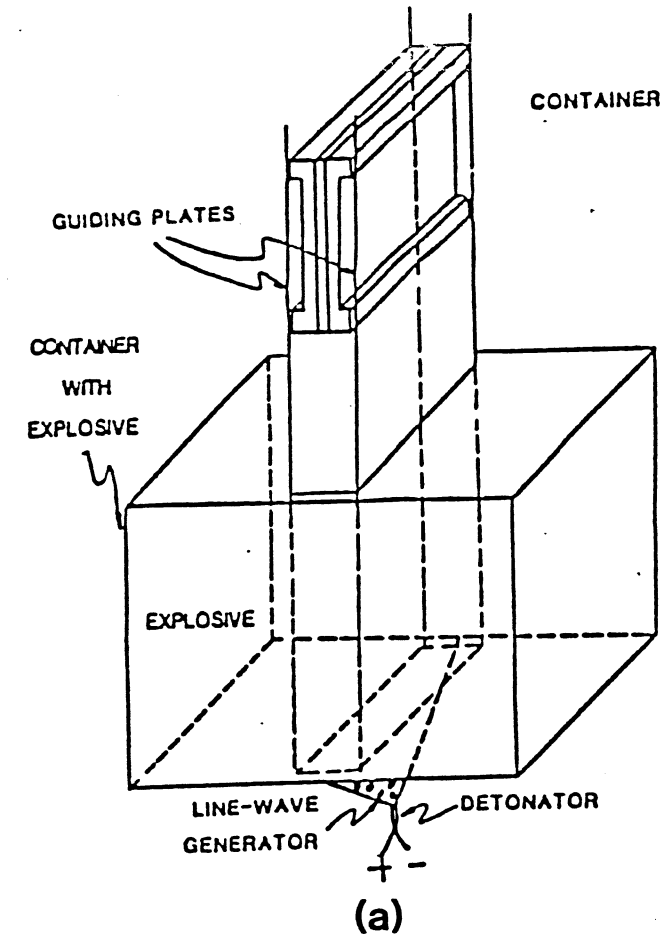

12. High temperature set-up for plate geometry. (a) Containers placed above explosive system; (b) containers lowered into explosive assembly.

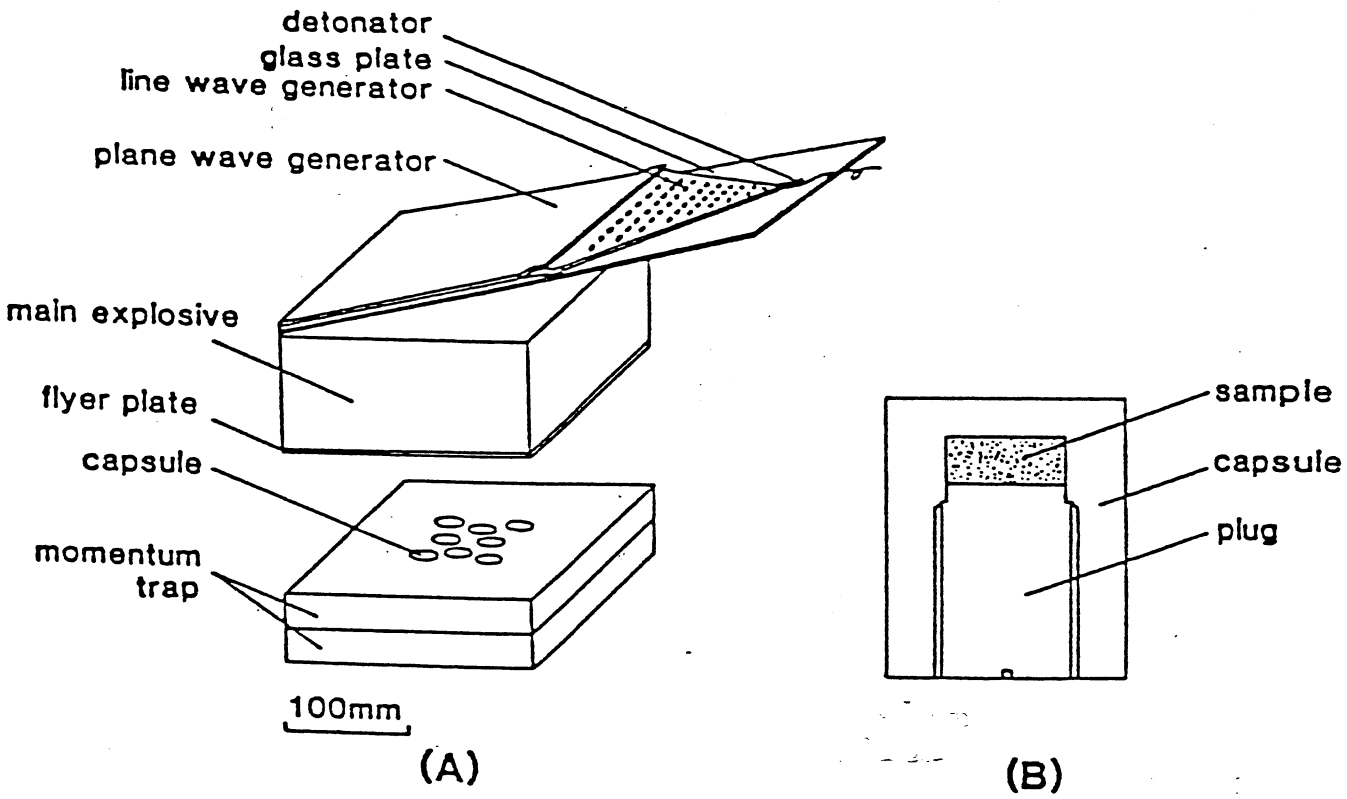

13. (a) Fixture configuration and explosive assembly for high-pressure-shock experiments (Sawaoka fixture)
(b) capsule for containing powders.

CROSS-SECTION

OF

EXPERIMENTAL SET-UP

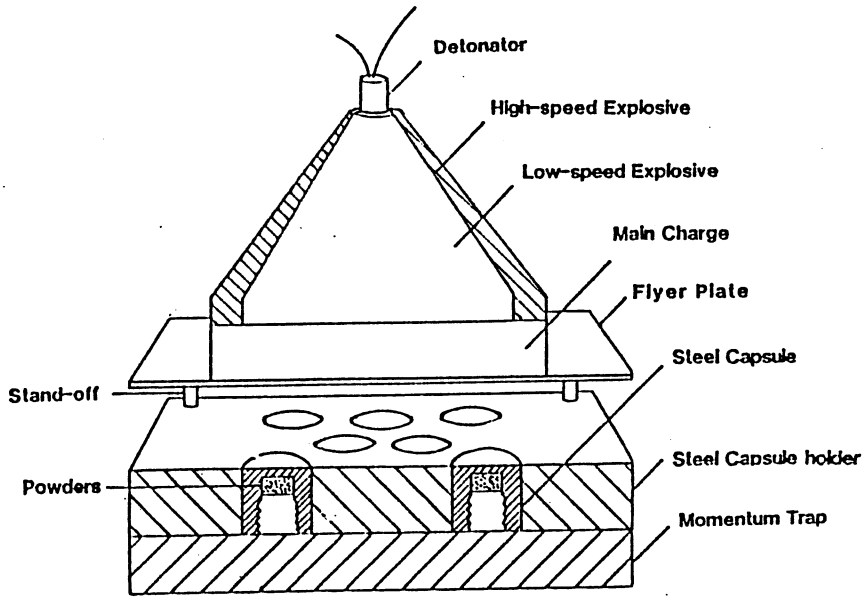

14. Modified version of Sawaoka fixture employing flyer plate acceleration with a CETR designed plane wave lens.

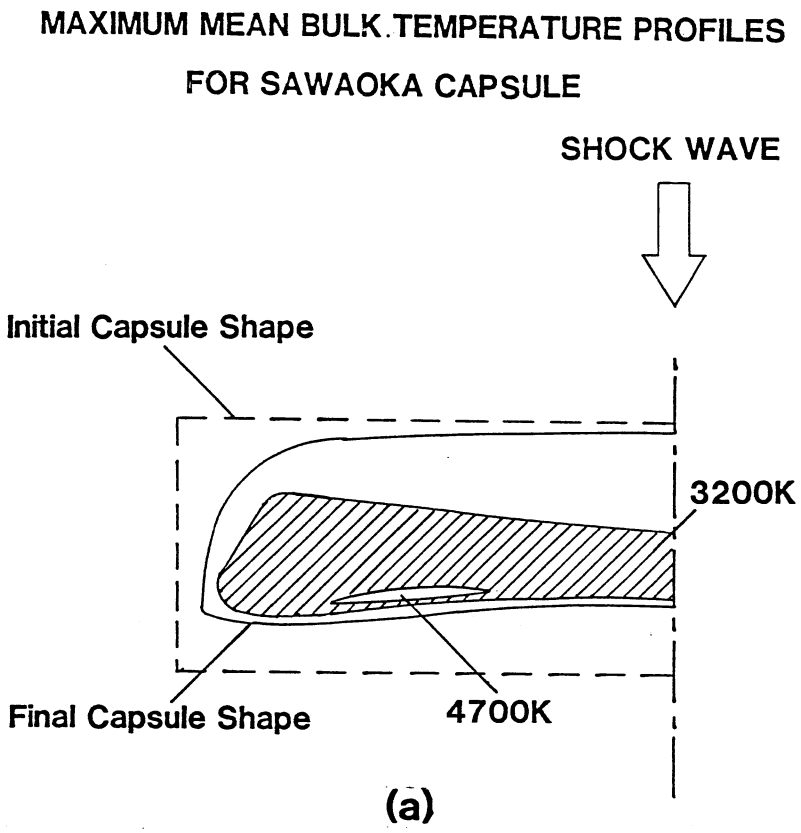

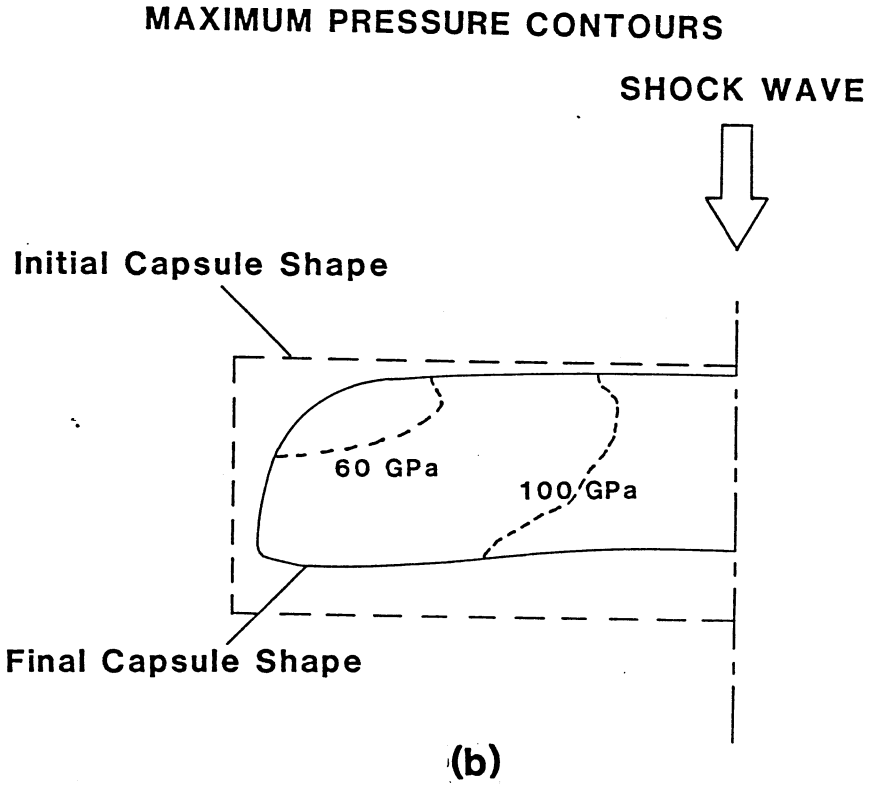

15. Contours of maximum mean bulk (a) pressure and (b) temperature within the sample cavity, obtained from two-dimensional CSQ computer code.

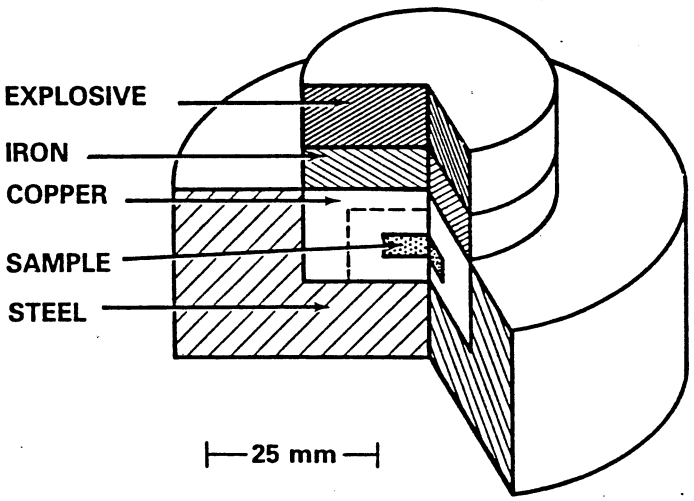

16. Section view of Sandia explosive compaction fixtures.

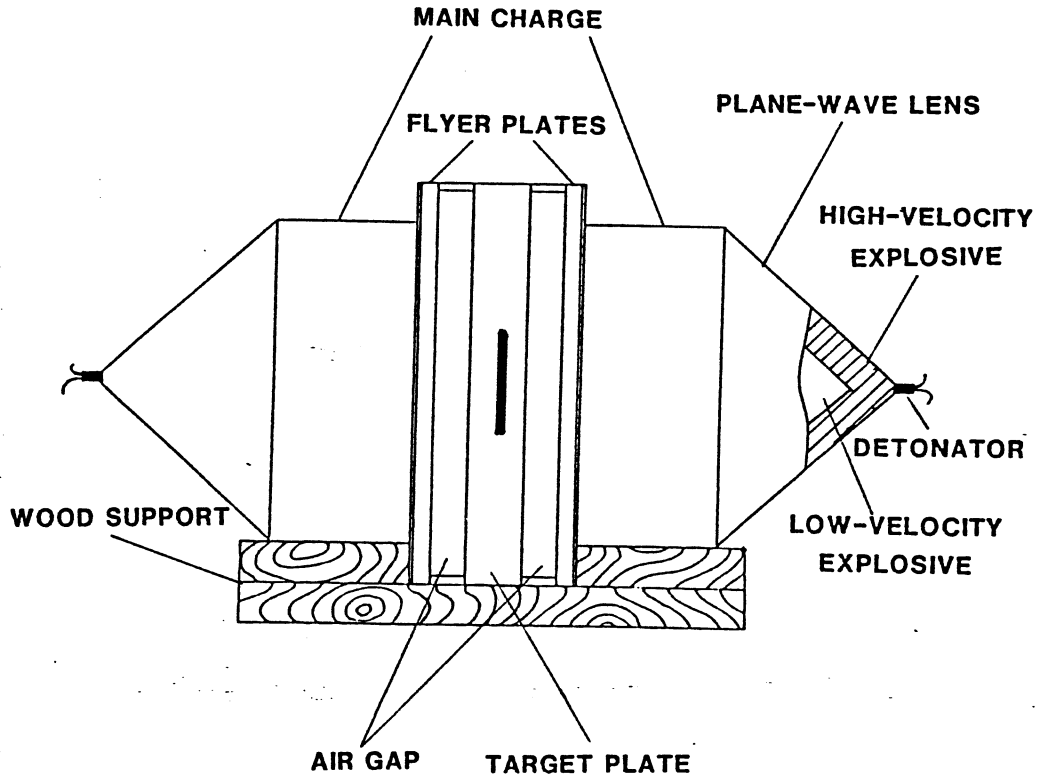

17. Schematic of experimental set-up employing the shock collision geometry for generating very high peak pressures (Yoshida fixture).

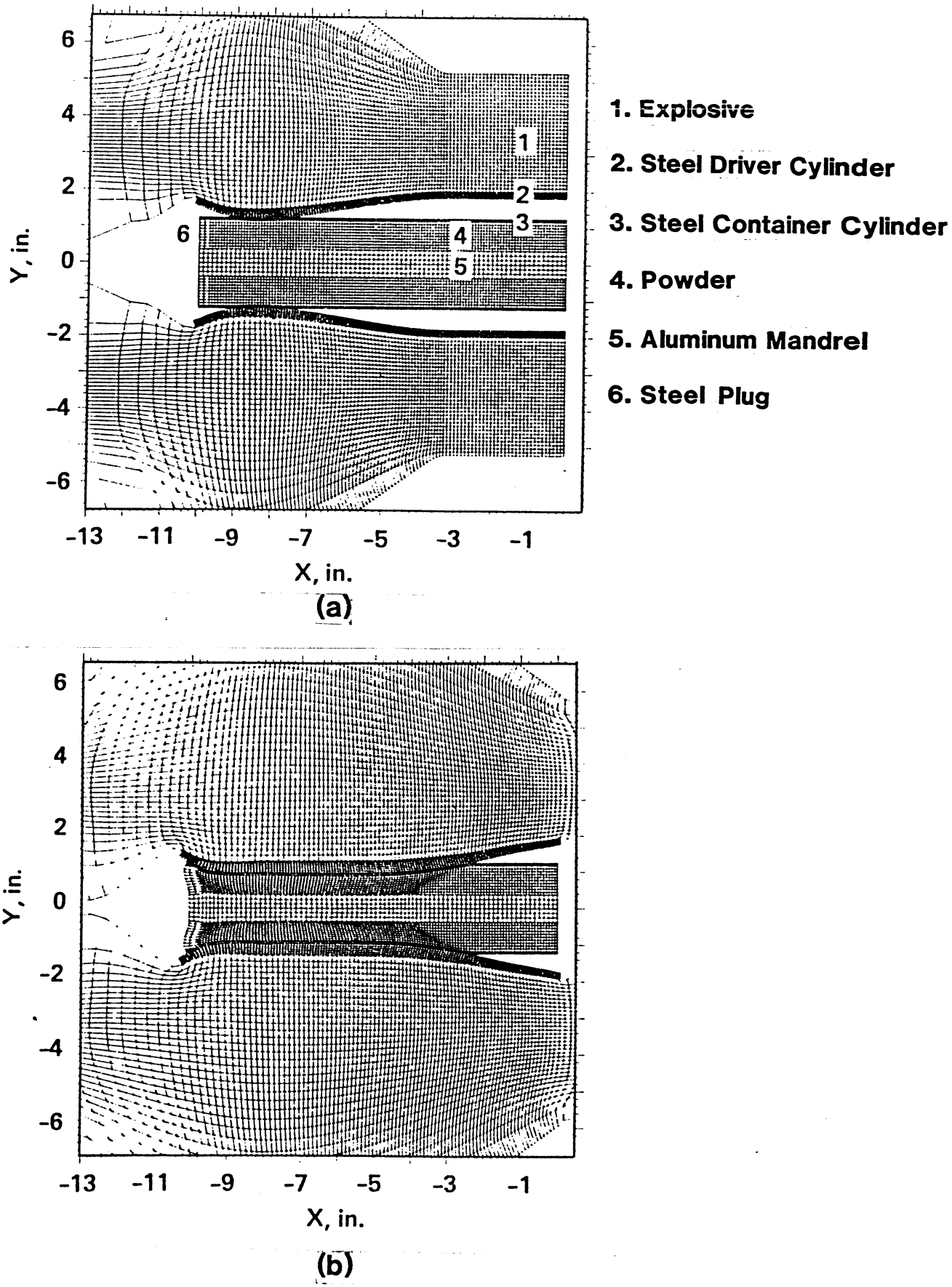

18. Calculation of the collapse of a steel cylinder onto a cylinder containg the powder to be compacted using the HEMP Code (from Wilkins et al. [20]).

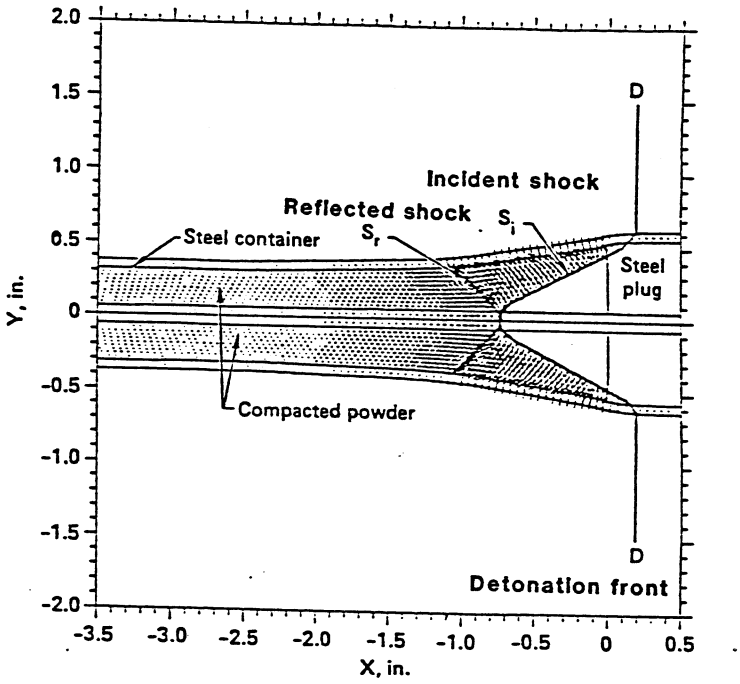

19. Calculated velocity vectors in ALN consolidated in plate geometry using the HEMP code (From Wilkins et al. [20]).

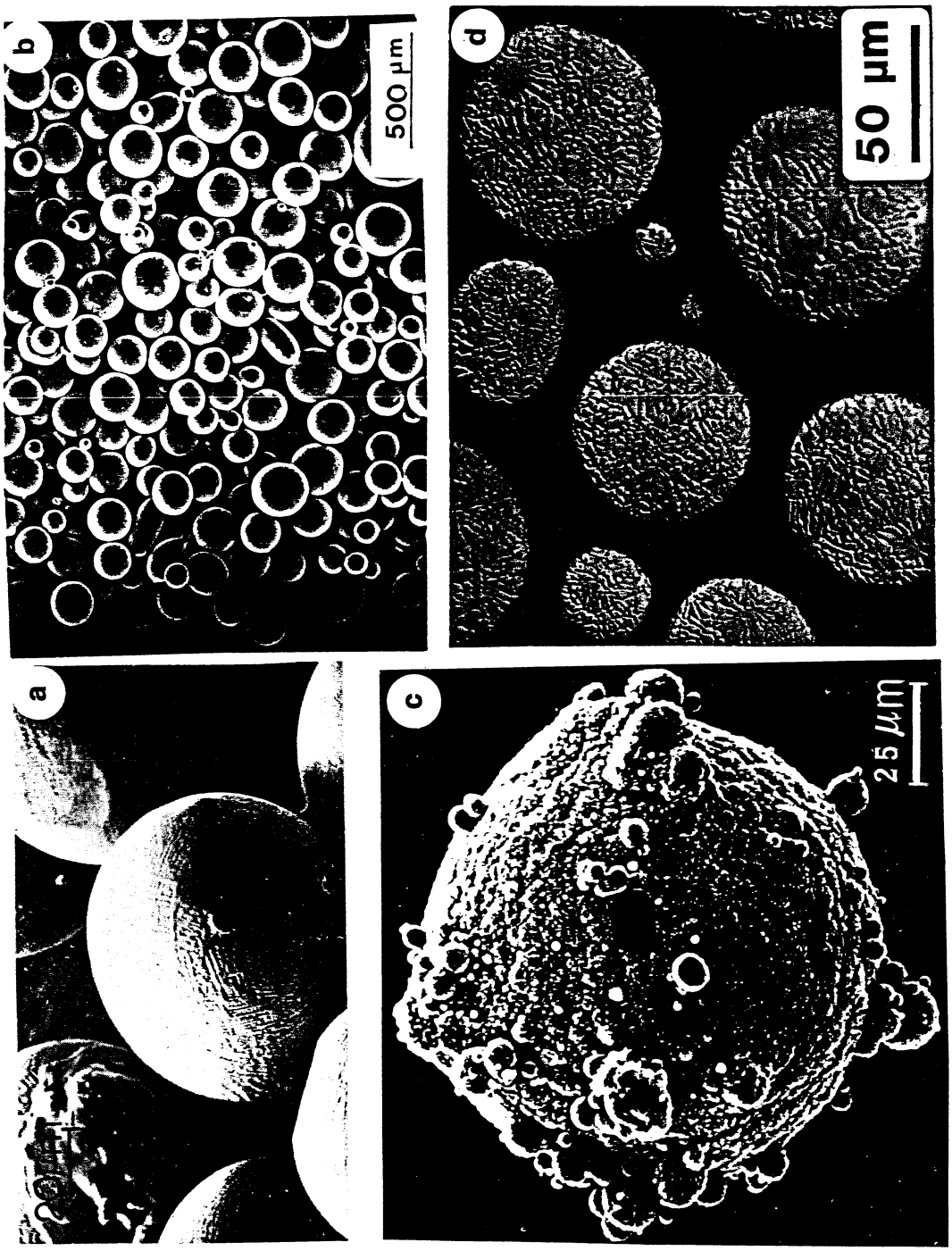

20. General morphology of rapidly solidified metal powders; (a) MAR M-200, (b) Ti-17, (c) Al-Li-Cu, (d) section of Ti_3Al showing microcellular structure, (e) IN-718, (f) section of IN-718 showing microdendritic structure.

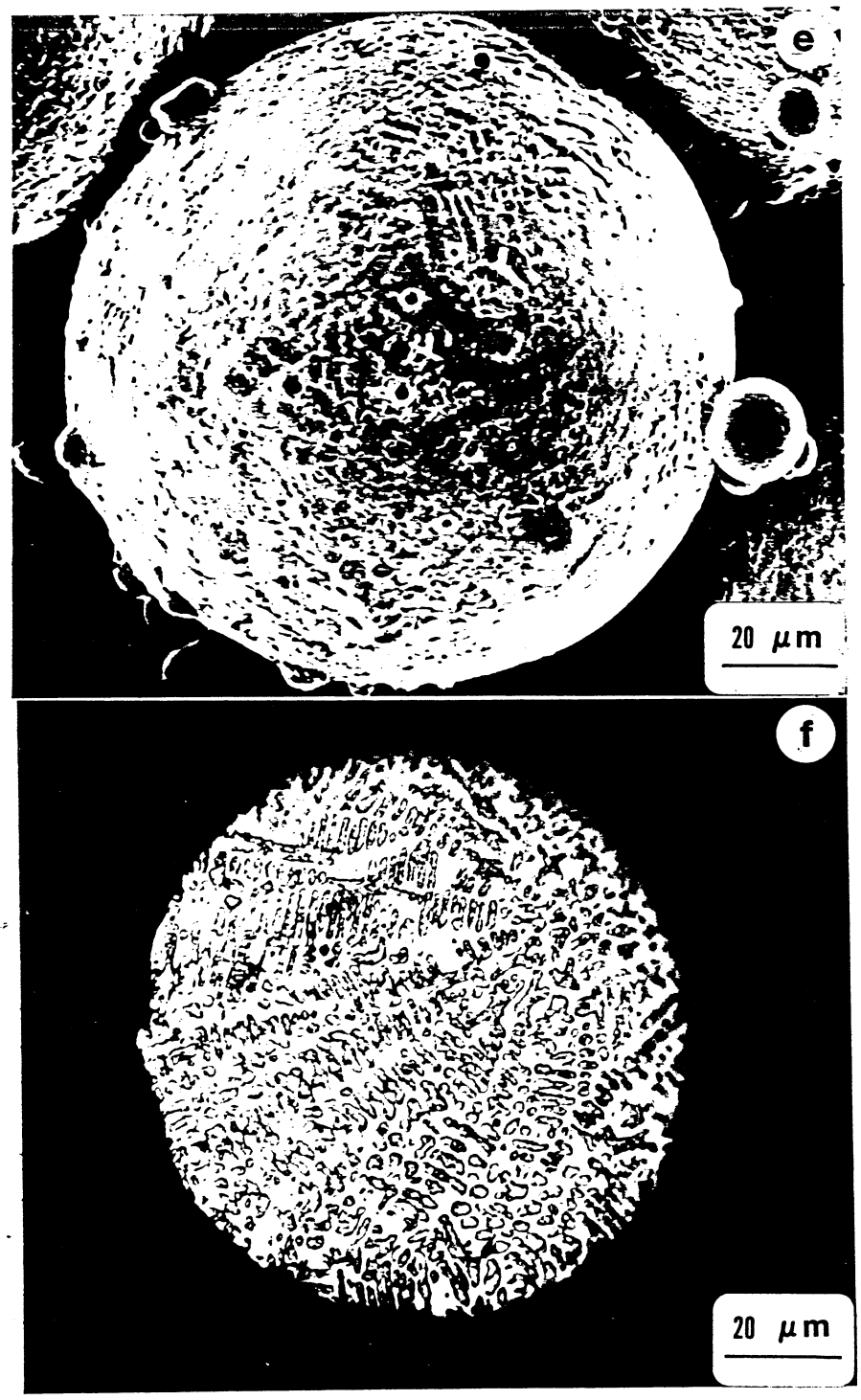
e
20 μm
f
20 μm

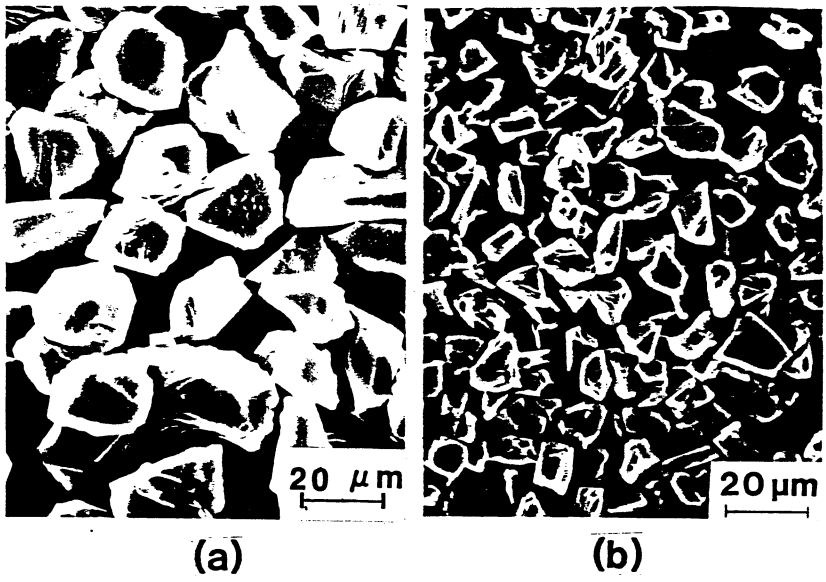

21. SEM of general morphology of ceramic powders (a) 10-20 um grade diamond powder, b) 40-60 um grade c-BN powder.

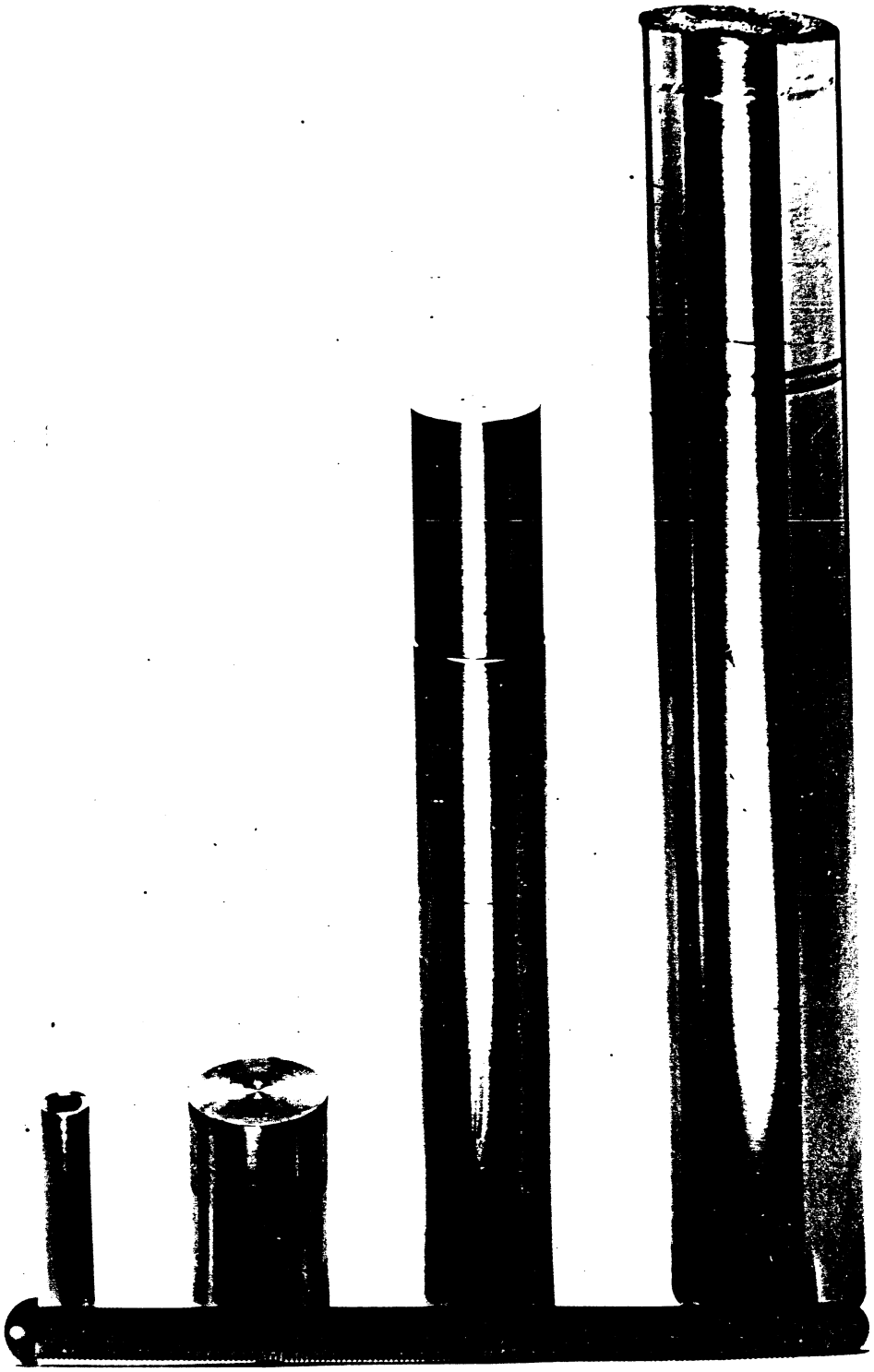

(a)

22. (a) Shock consolidated Ti-alloy cylinders of different sizes.
(b) Shock consolidated IN 718 superalloy hollow cylinder.

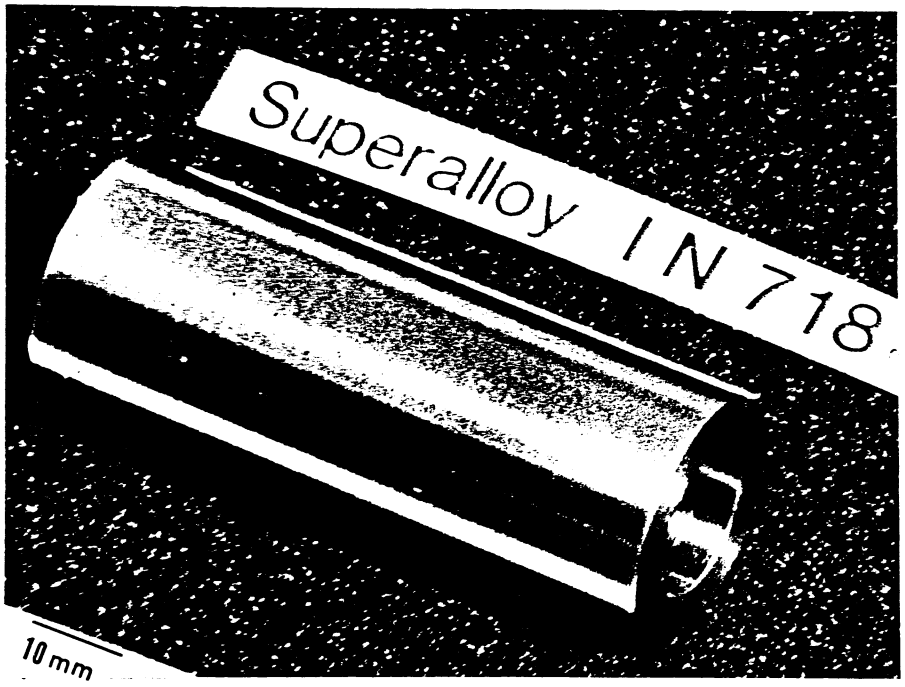

(b)

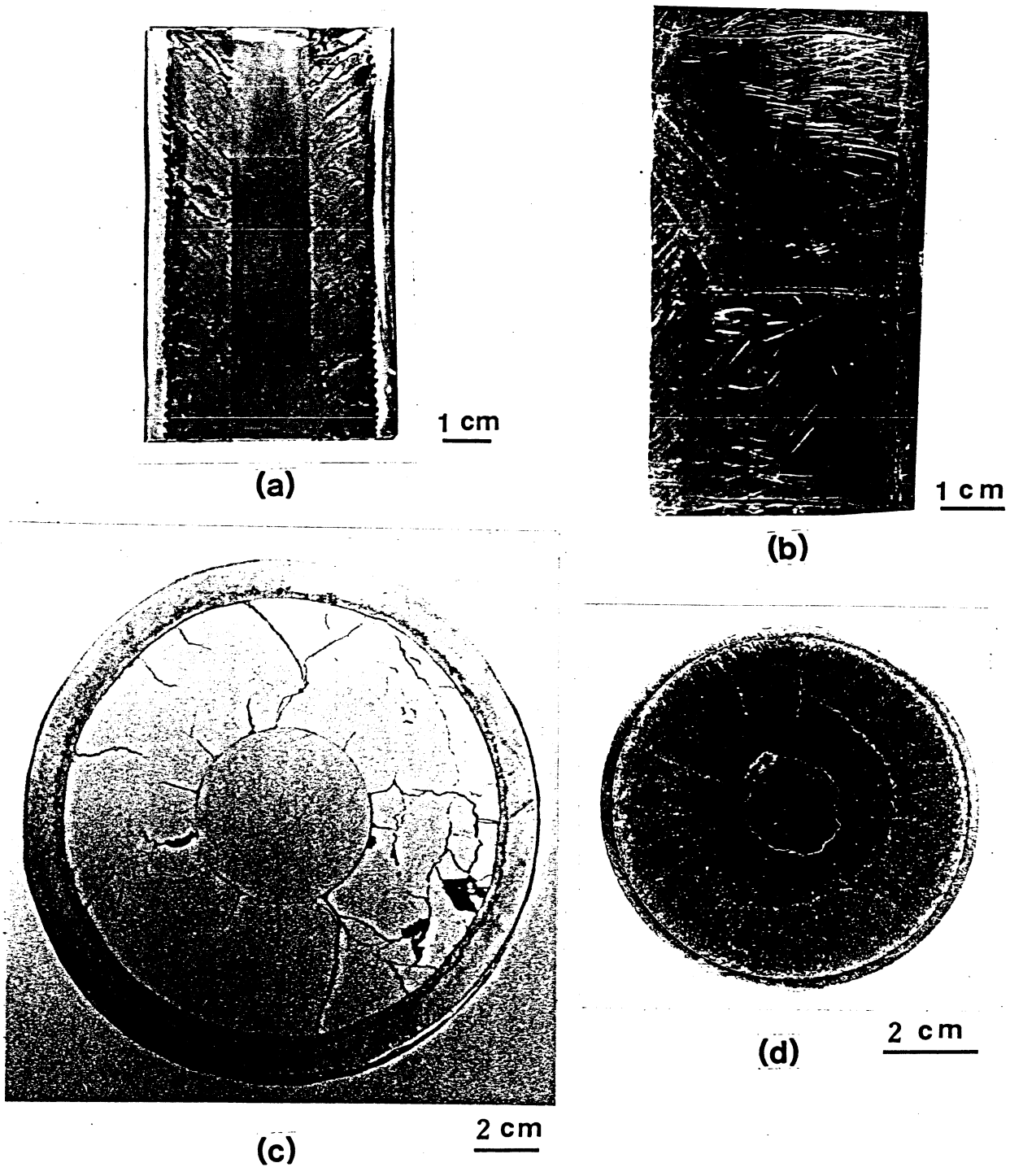

23. Macrophotographs of longitudinal sections of shock consolidated Ti-Al alloy showing (a) spiral and (b) transversal cracking. Additional cracks often observed in shock-consolidated cylinders: (c) radial cracks, (d) circumferential cracks.

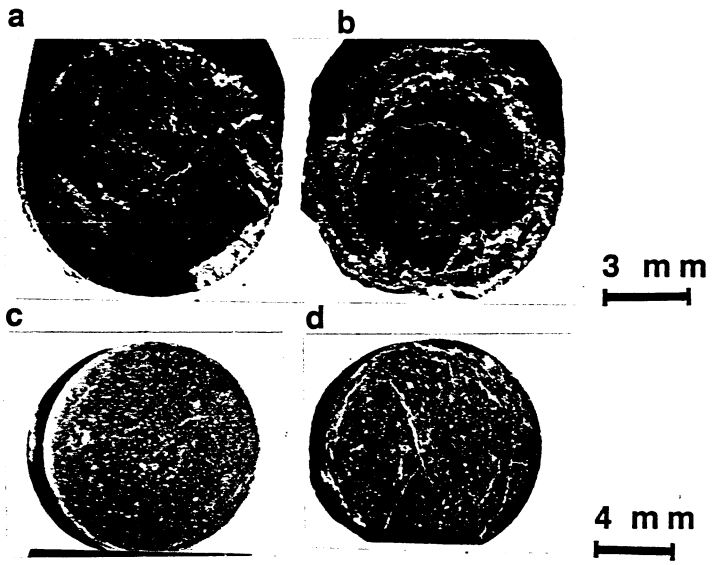

24. Section views of typical top (impact) and bottom (non-impact) surfaces of shock consolidated (a)-(b) diamond powder and (c)-(d) c-BN powder compact.

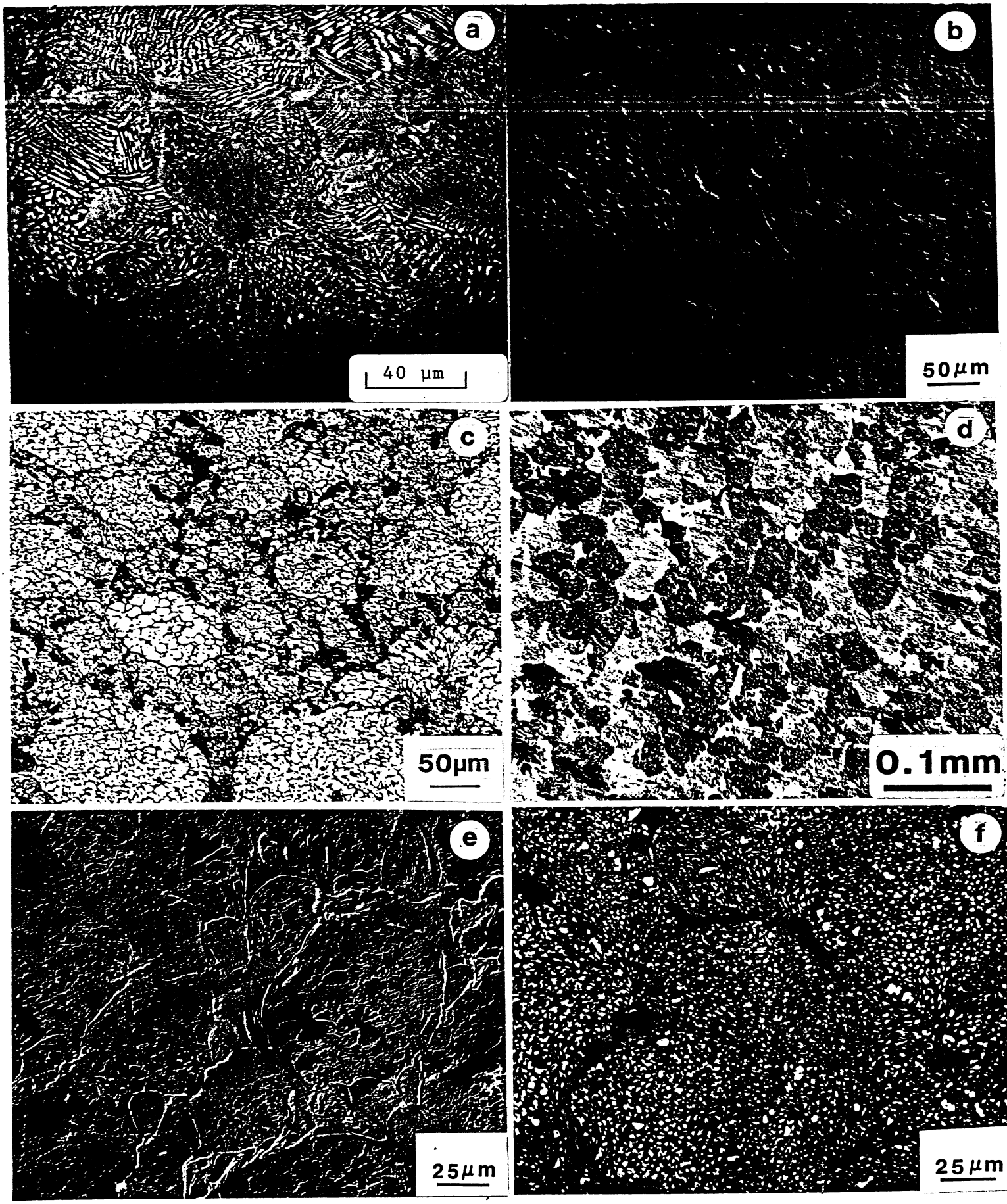
a
40 μm
b
50μm
c
50μm
d
0.1mm
e
25μm
f
25μm

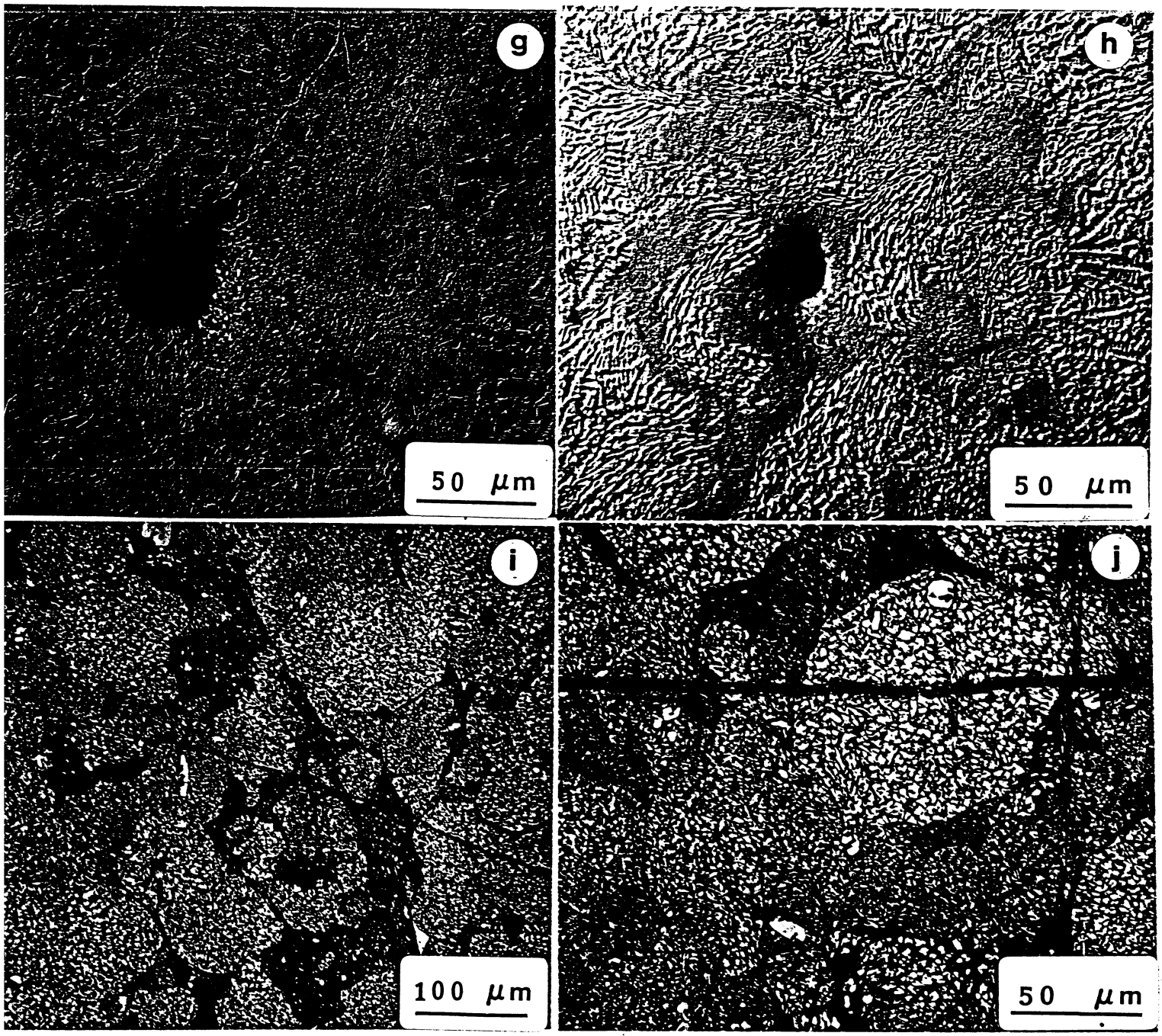

25. Optical micrographs of well consolidated alloys (a) MAR M-200, (b) IN 718, (c) Al-Li-Cu, (d) Ti-17, (e) Ti_3Al, (f) TiAl Flaws in well consolidated alloys, (g)-(h) solid fraction voids in the Ti_3Al and Mar M 200, respectively, (i)-(j) transparticle cracks in TiAl.

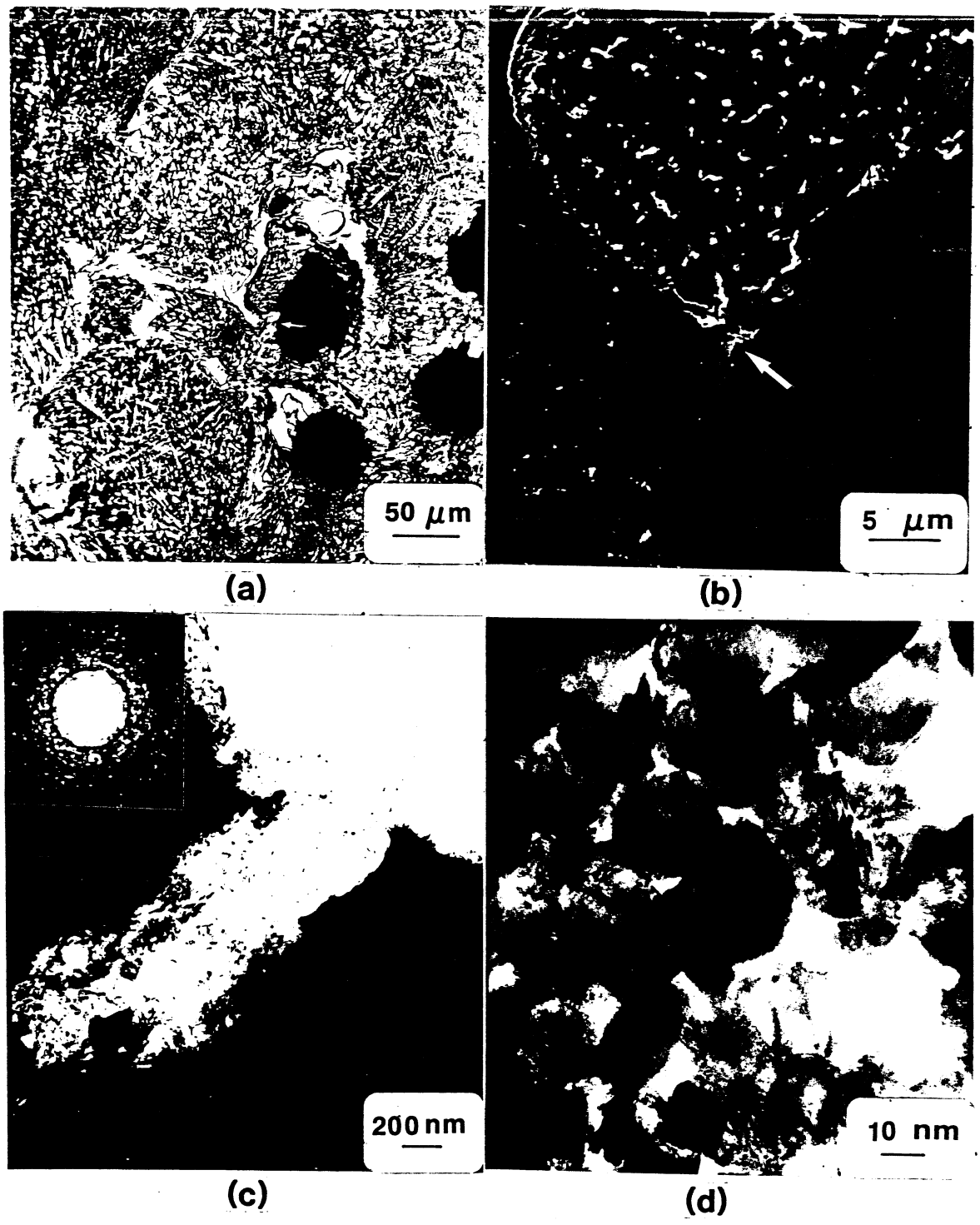

26. Transmission electron micrographs showing interparticle melting region in superalloy IN 718,
(a) optical micrograph showing perforation, white interparticle regions, and region observed in transmission electron microscope
(b) higher magnification of (a) in TEM
(c) diffraction pattern showing microcrystalline structure
(d) transmission electron micrograph showing microcrystals with diameters of 20-50 nm.

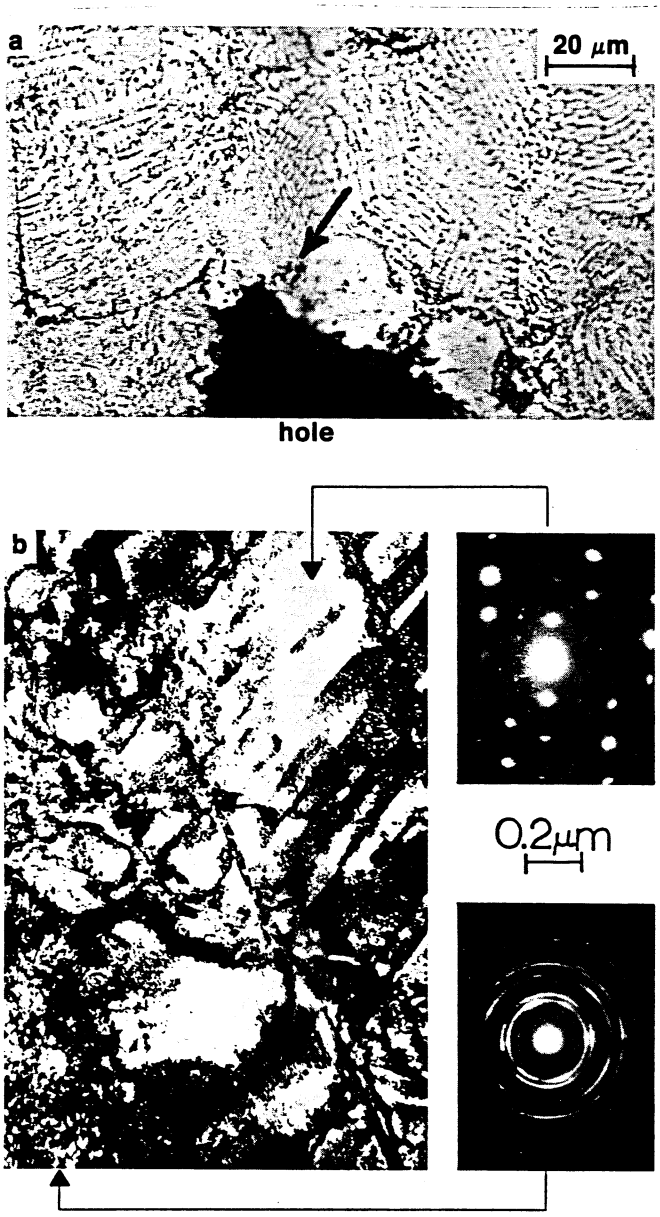

27. TEM image showing interface between melted and resolidified particle surface and unmelted particle interior in MAR M-200(from [32]).

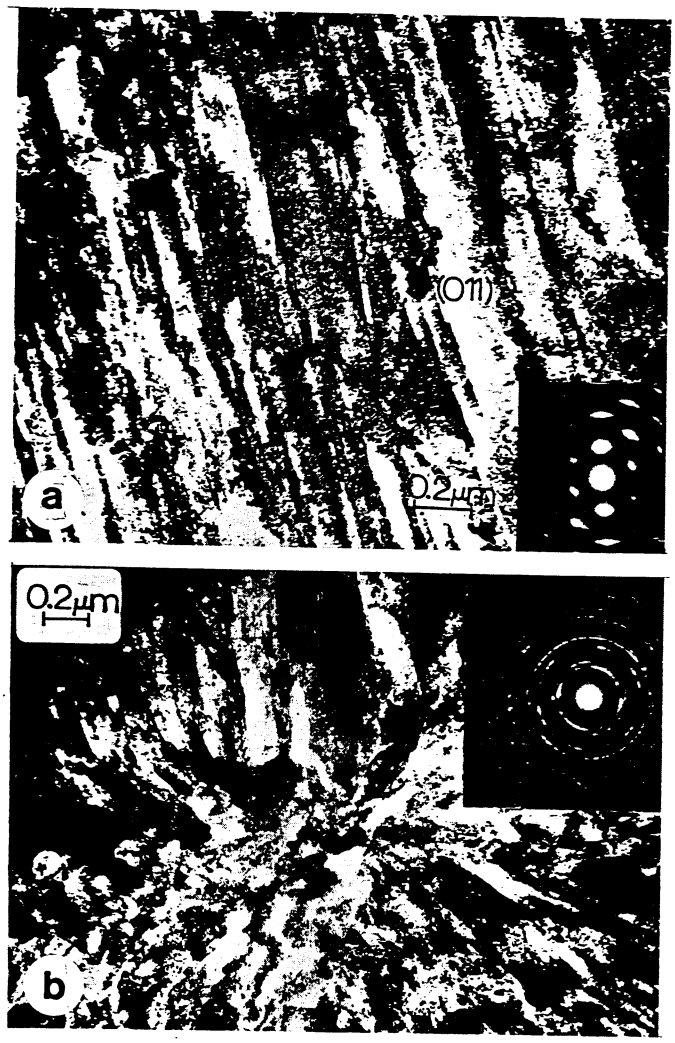

28. (a) TEM image showing extensively deformed particle interior, and (b) TEM image and SAD pattern showing evidence of melted and resolidified interparticle region.

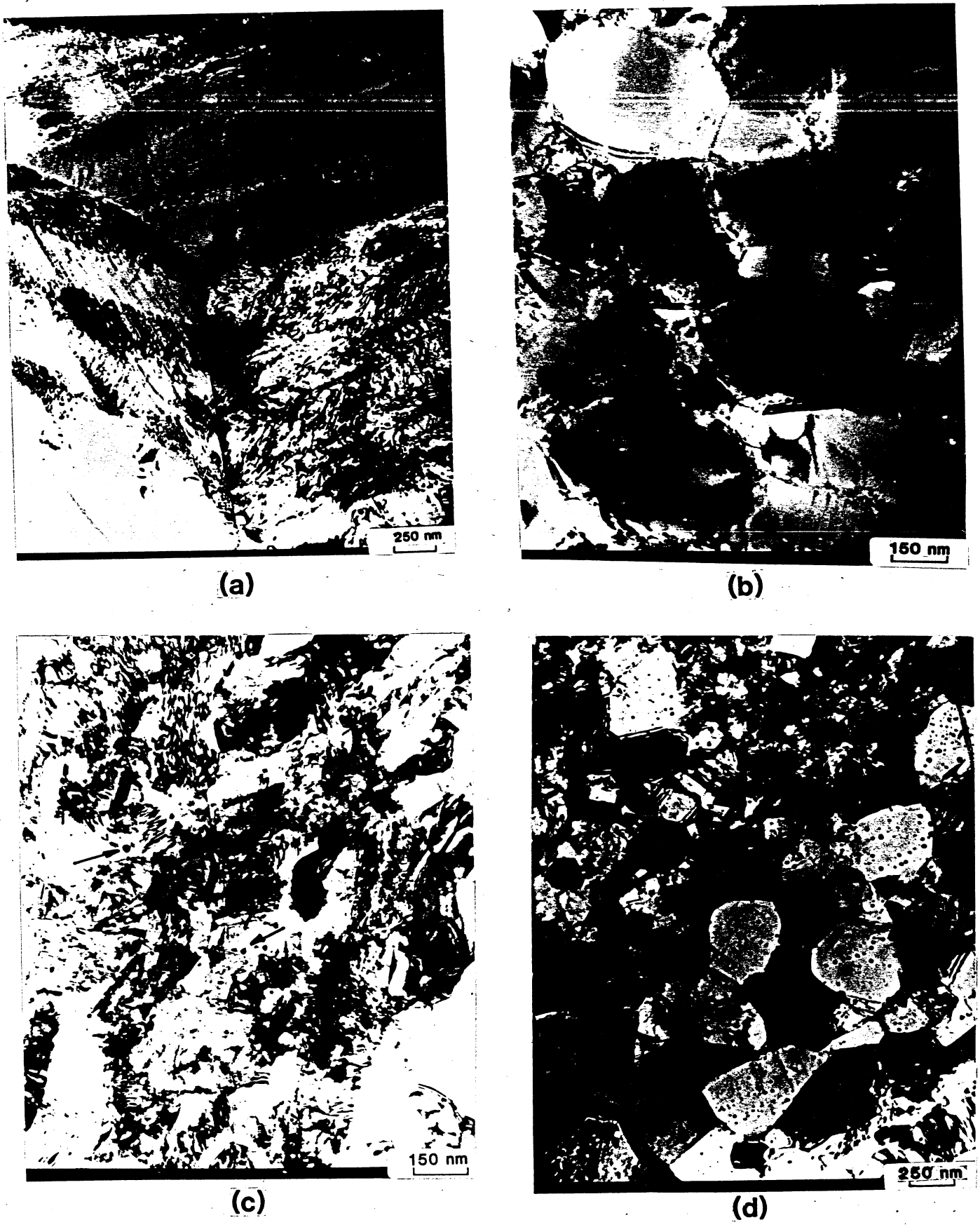

29. Transmission electron micrographs of shock consolidated titanium alloys; (a) well-developed dislocation substructure in Ti-17 particle interior (b) interparticle melting region having microcrystalline and dislocation-free grains in Ti-17 alloy, (c) Erbia dispersion after onsolidation in Ti-6242 + Er alloy, (d) uniform erbia dispersion in shock consolidated and aged Ti-6242+ Er alloy.

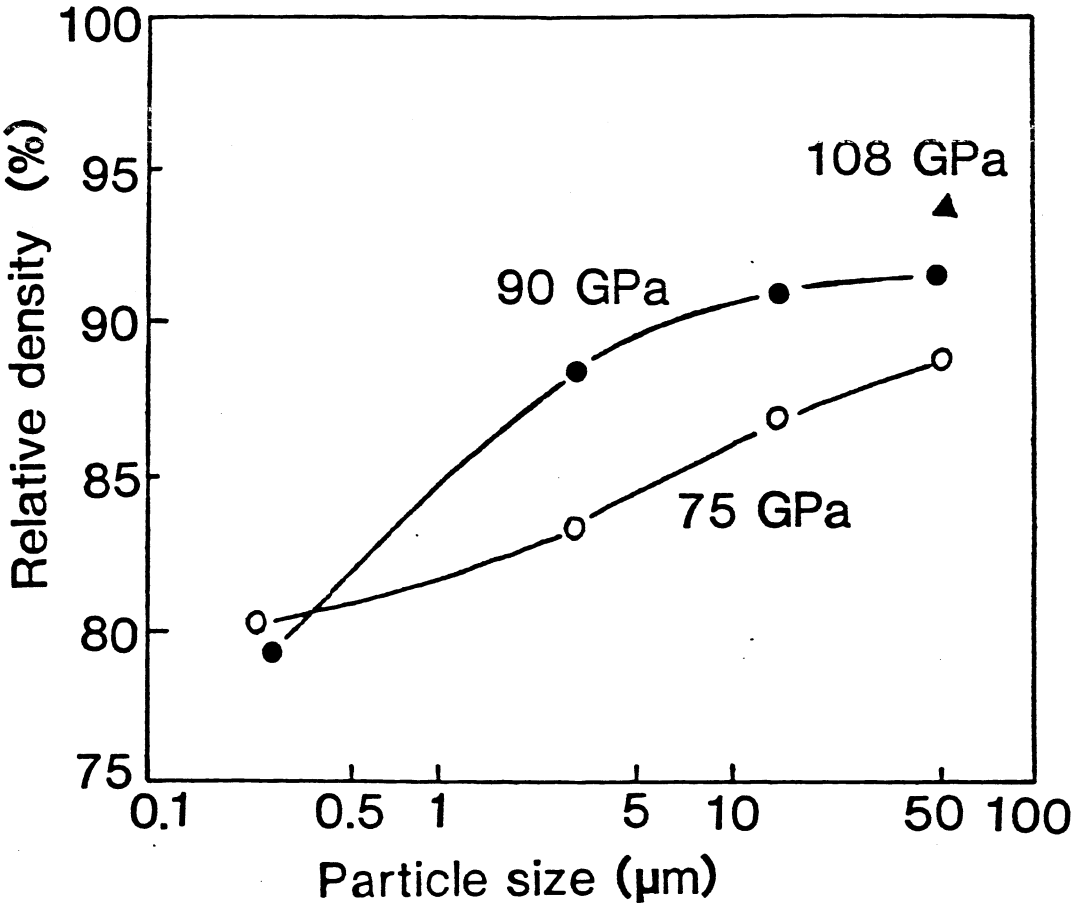

(a)

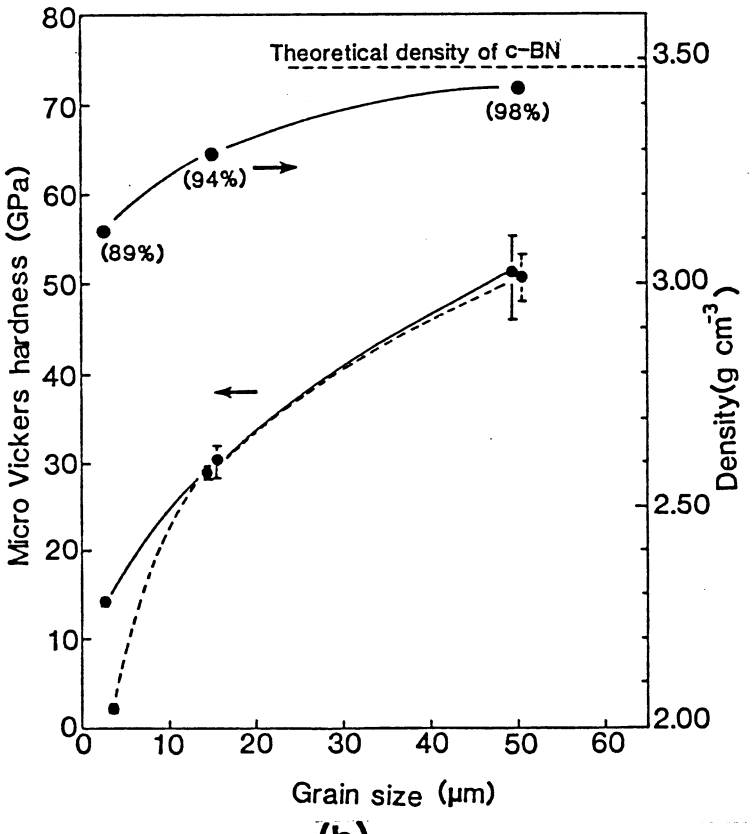

(b)

30. Dependence of relative density of shock compacted (a) diamond, and (b) c-BN powders on the respective particle

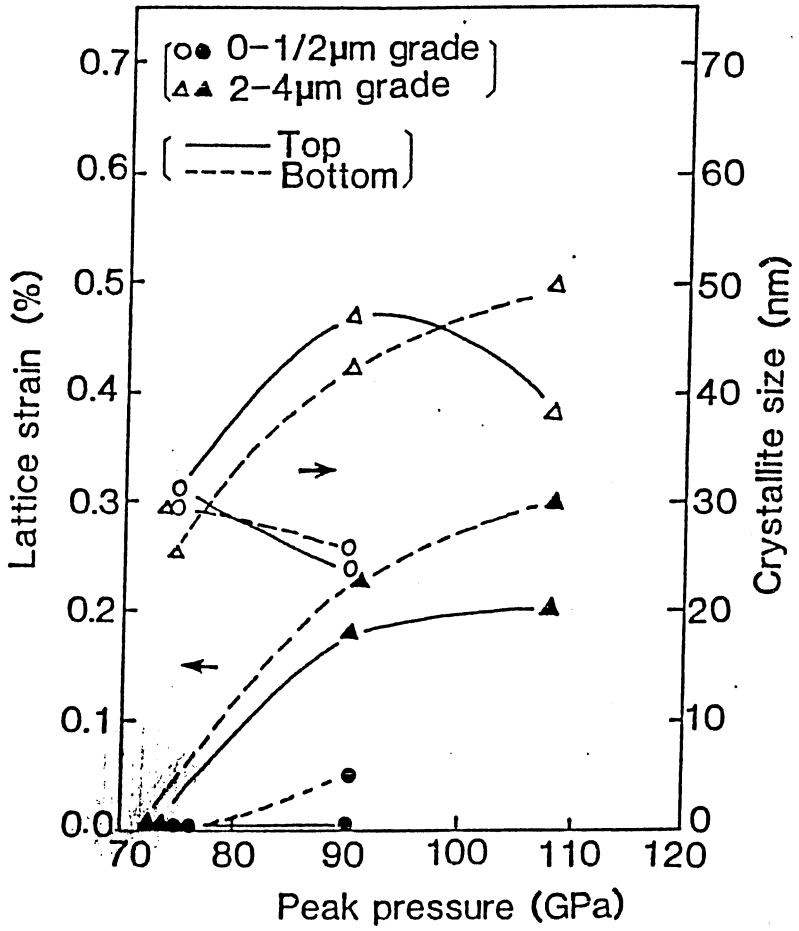

(a)

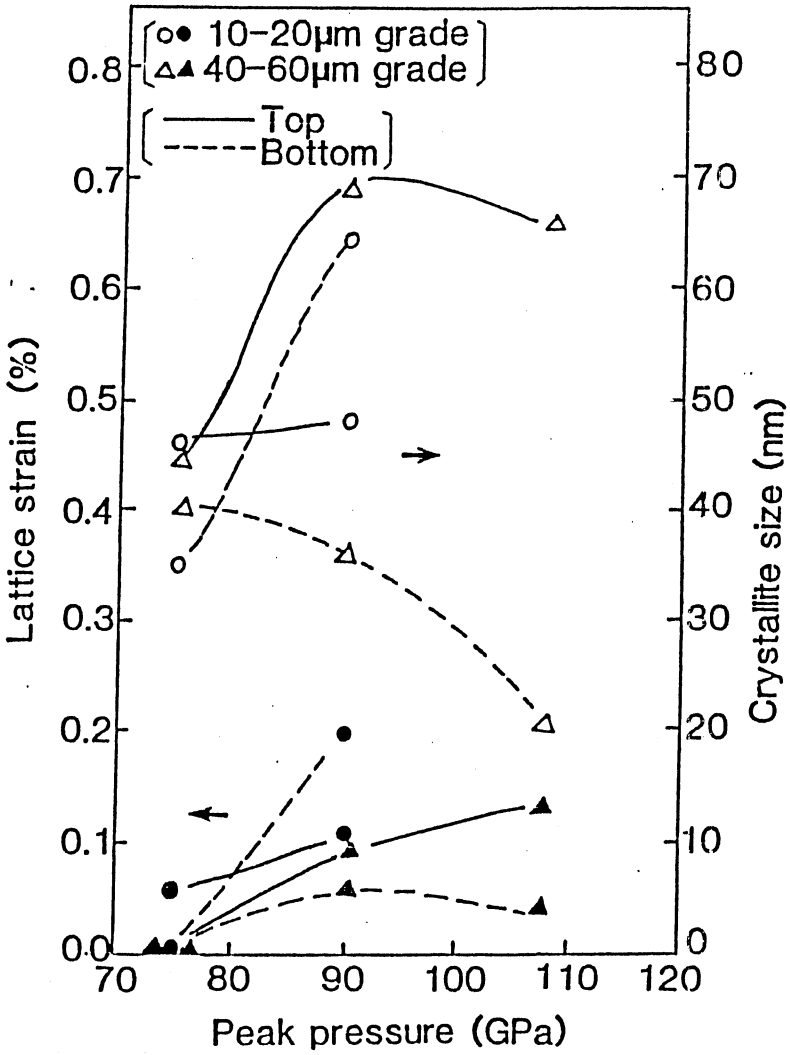

(b)

31. Residual lattice strain and crystallite size in shock compacted (a) 0-0.5 um and 2-4 um grade; and (b) 10-20 um and 40-60 um grade diamond powder.

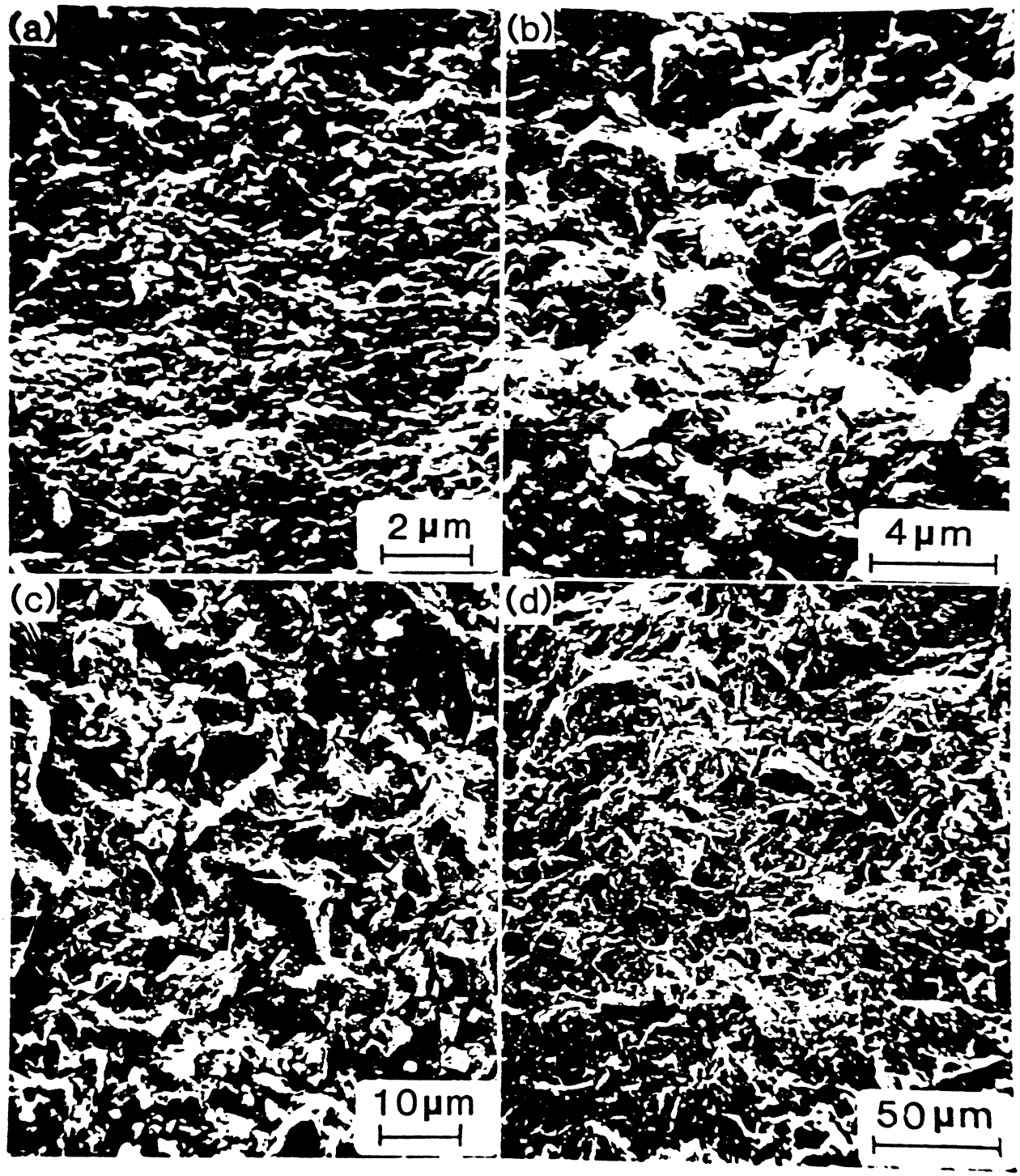

32. SEM photographs of fracture surfaces near the central region of the bottom (non-impact) surfaces of (a) 0-1/2 um, (b) 2-4 um, (c) 10-20 um, and (d) 40-60 um grade powders, compacted at 90 GPa.

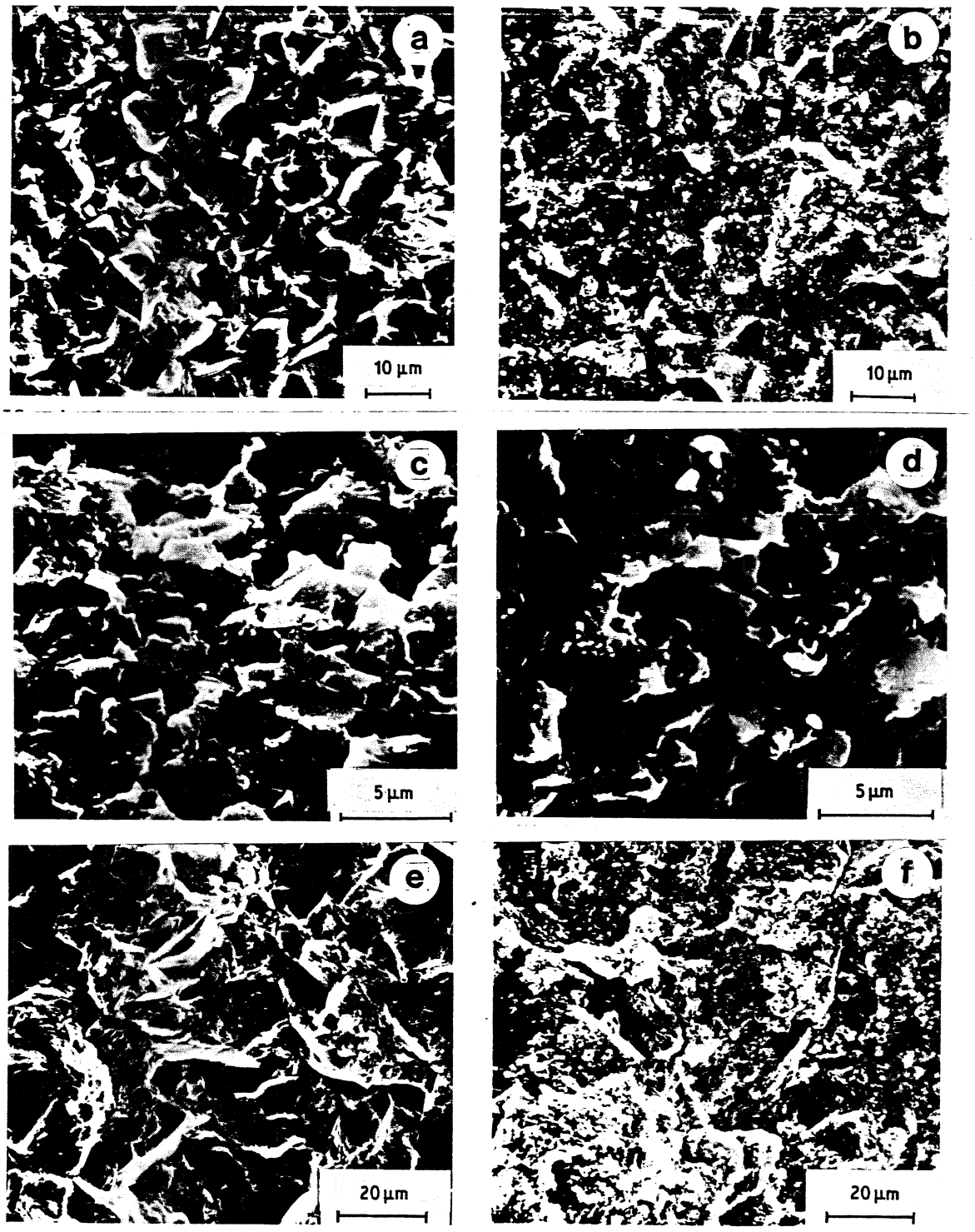

33. SEM micrographs of fracture surfaces of top and bottom regions of compaced c-BN powders. (a)-(b) 2-4 um grade and (c)-(d) 10-20 um grade, (e)-(f) 50-60 um grade.

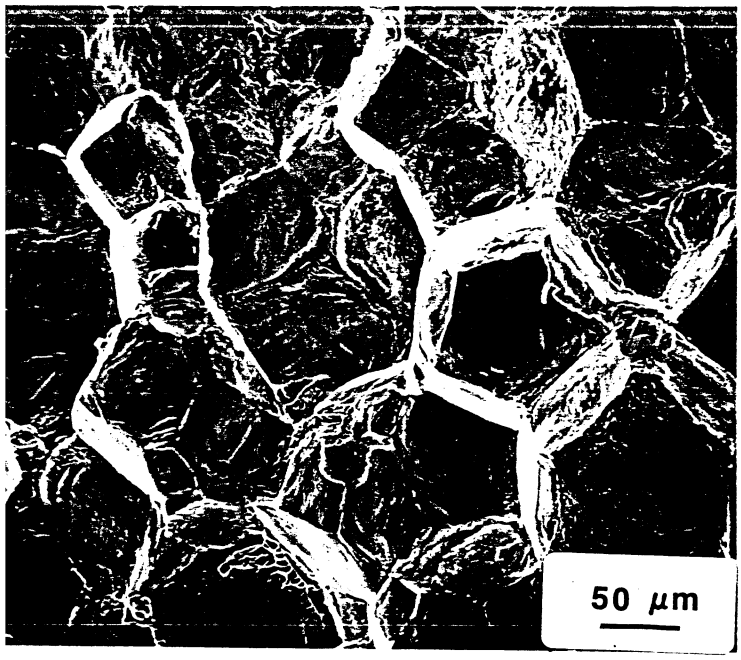

(a)

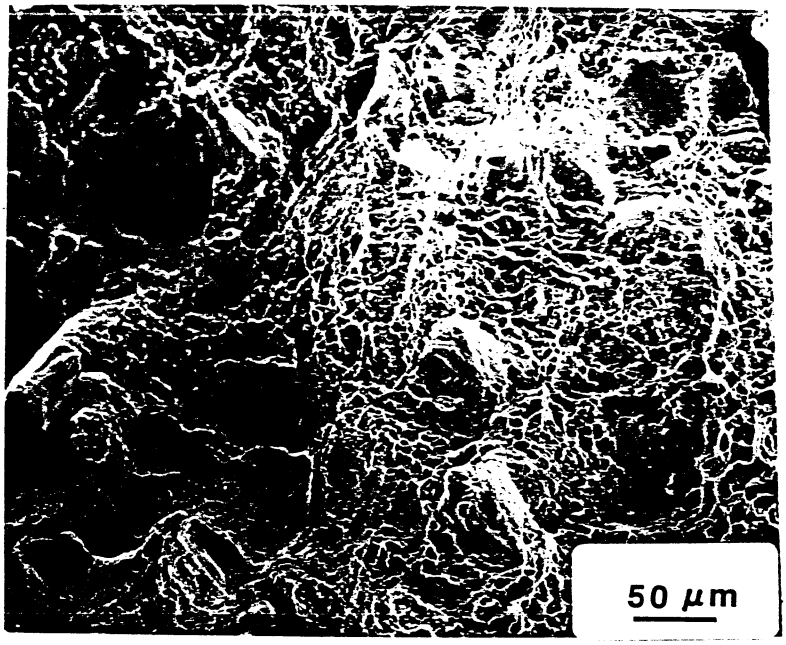

(b)

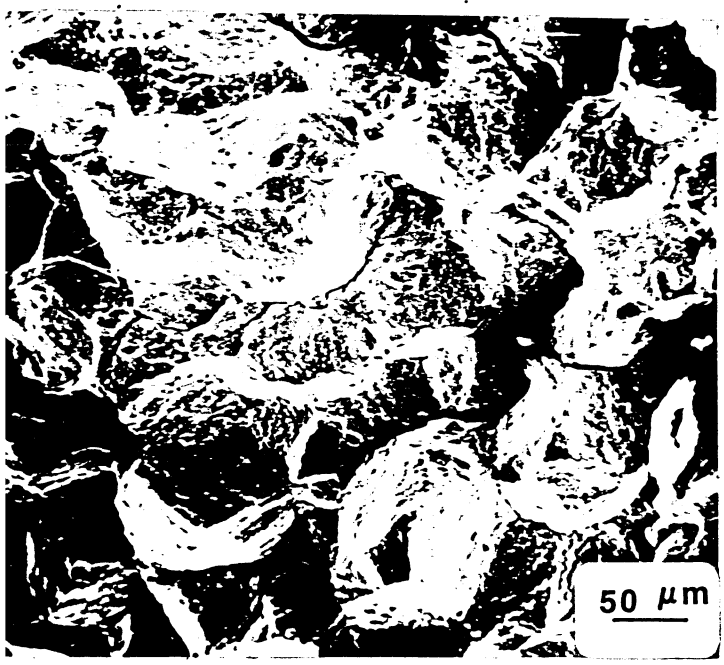

(c)

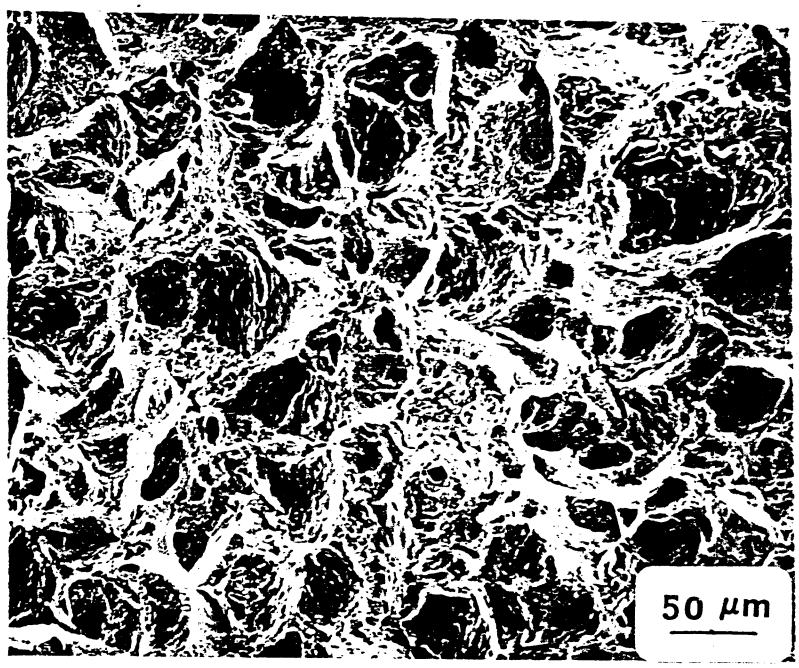

(d)

34. Scanning electron micrographs of (a) poorly bonded, (b) well bonded Ti-17 alloy, (c) poorly bonded IN 718, (d) well bonded IN-718.

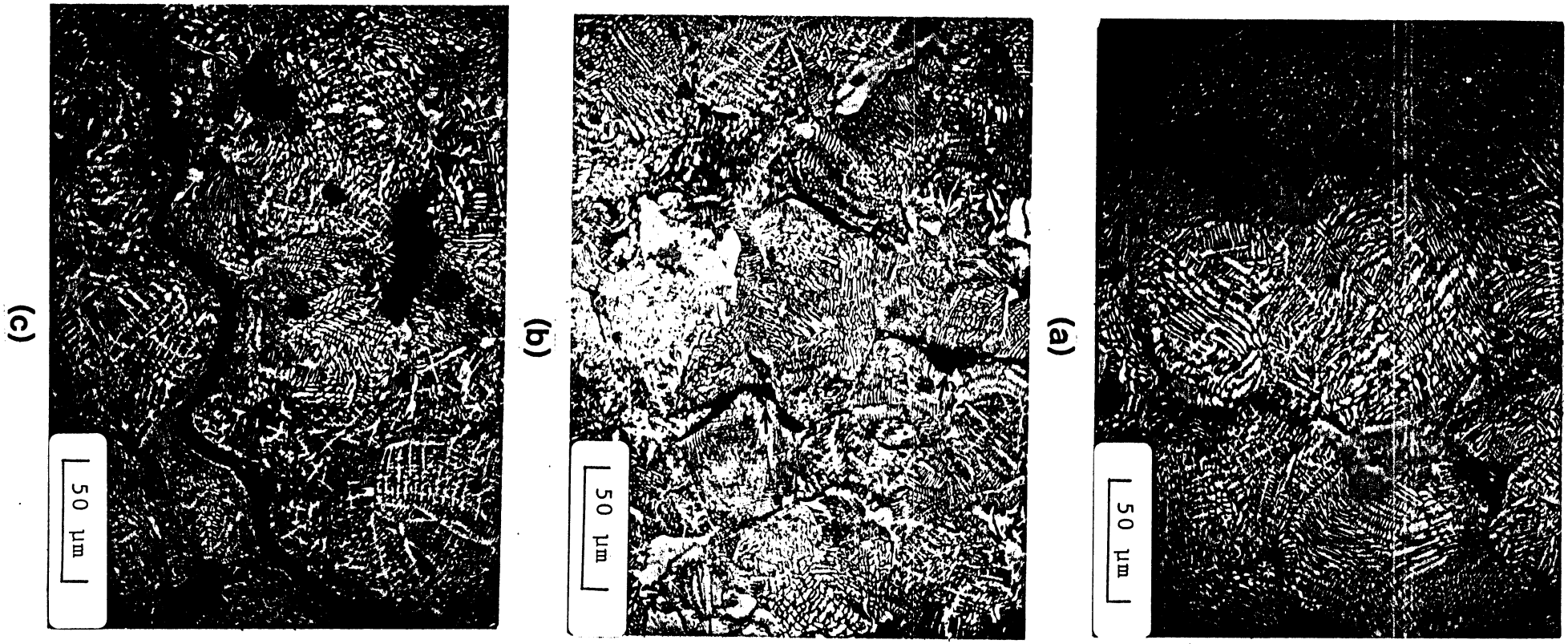

35. Fracture nucleation in MAR M-200 superalloy
    (a) Fracture initiation at void formed in interparticle melt region
    (b) microcracks between grains
    (c) intergranular cracks.

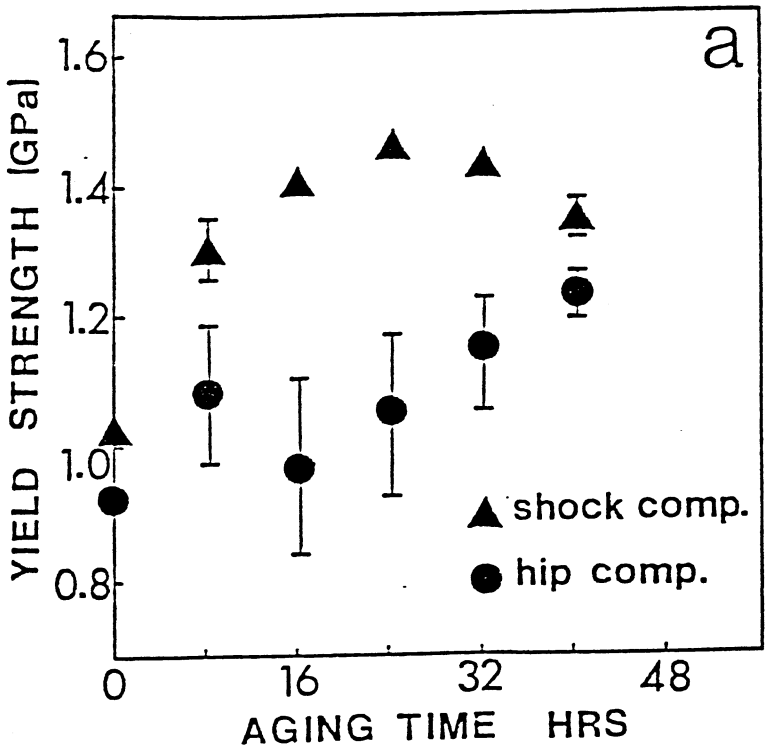

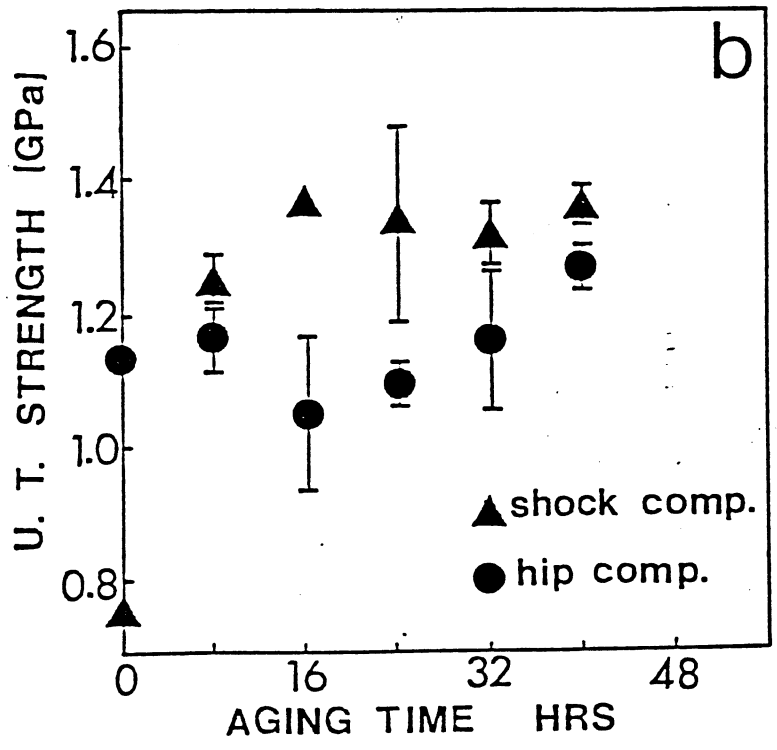

36. Tensile property comparison between shock consolidated and hot-isostatically-pressed Pyromet 718 alloy: (a) Yield strength versus aging time and (b) ultimate tensile strength versus aging time

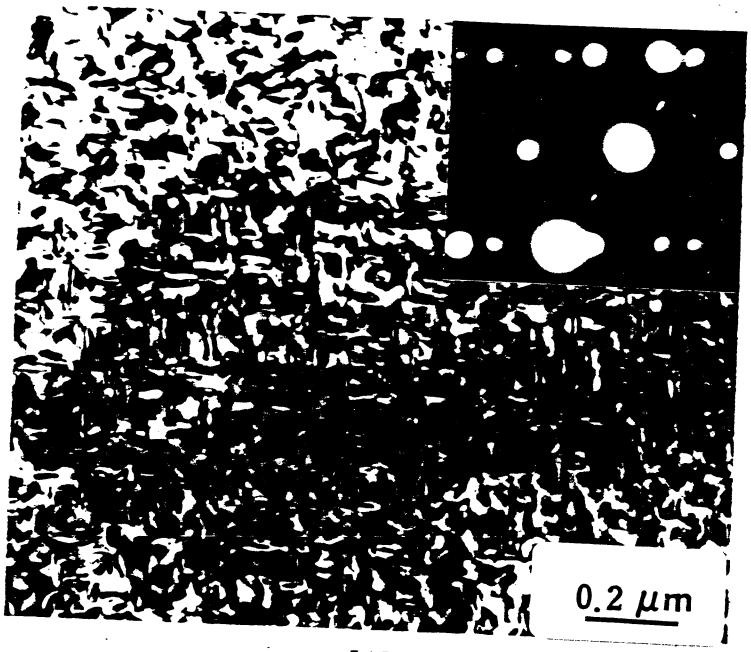

(a)

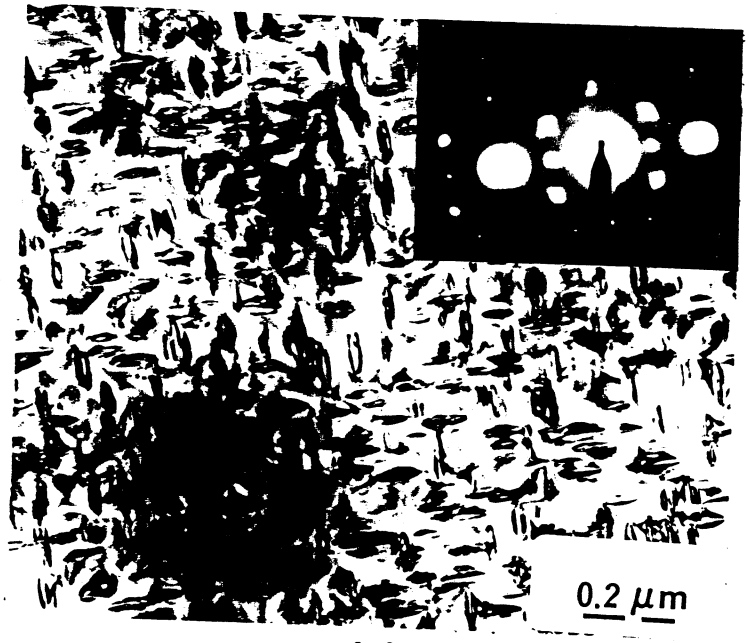

(b)

37. Bright field transmission electron micrographs of γ'' precipitates in (a) shock consolidated and (b) hot isostatically pressed Pyromet 718 alloy after shows of aging of 620°C.

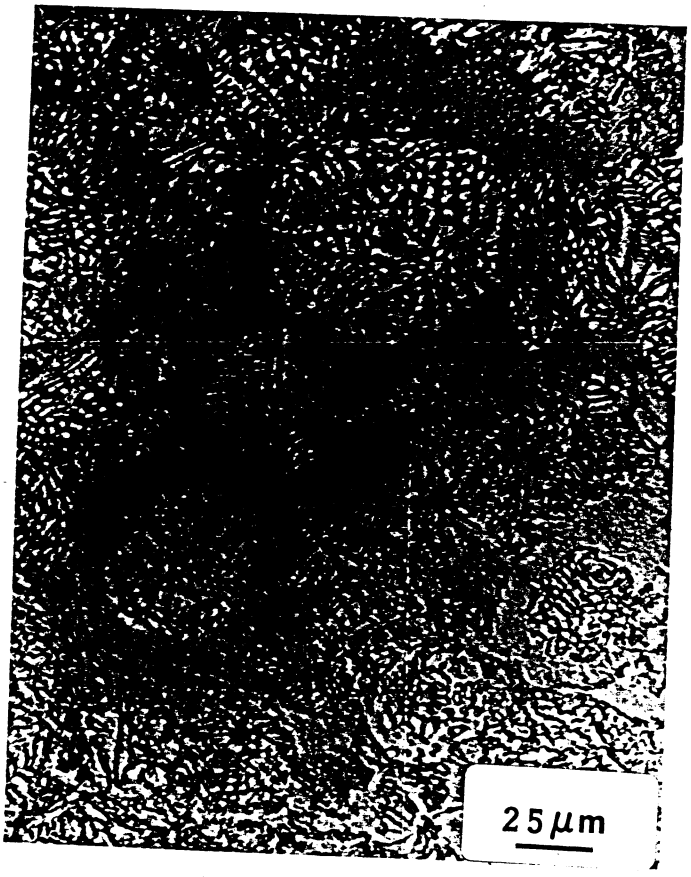

38. Optical micrograph of shock consolidated nickel based Pyromet alloy powders showing inter particle bonding behavior.

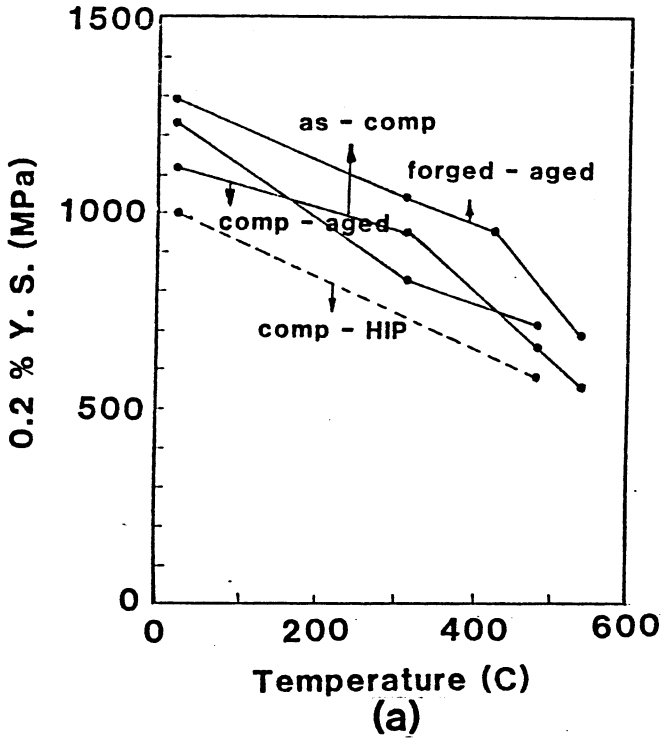

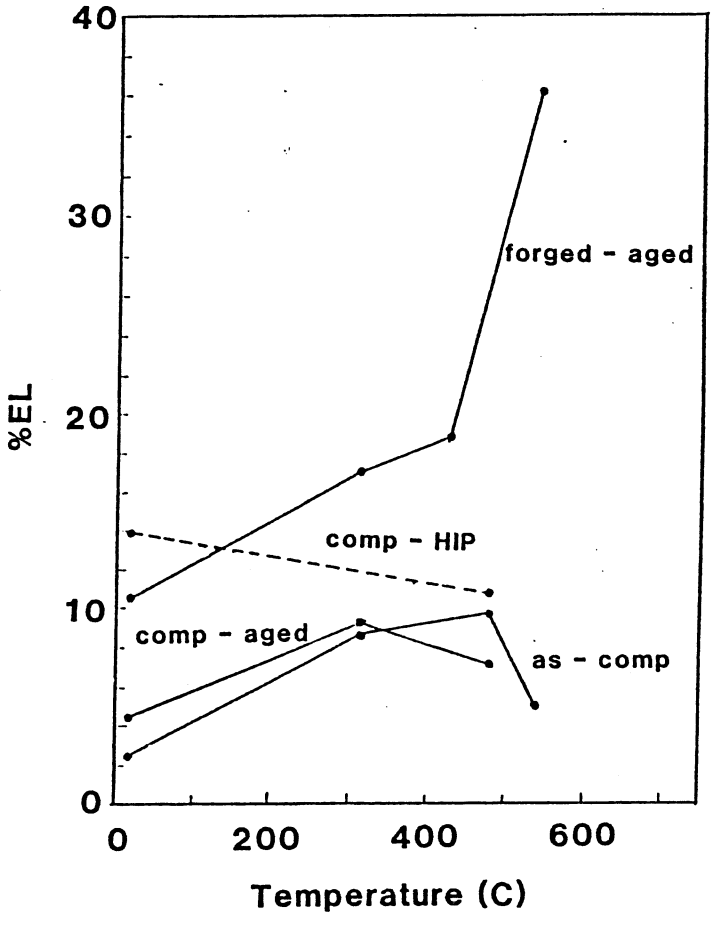

39. Variation of (a) yield stress and (b) total elongation with temperature for Ti-662 in shock-consolidated, shock consolidated + aged (570^{o}C/4 hours), shock consolidated + hipped conditions; forged + aged (570^{o}C/ 4 hours) matrial given for comparison.

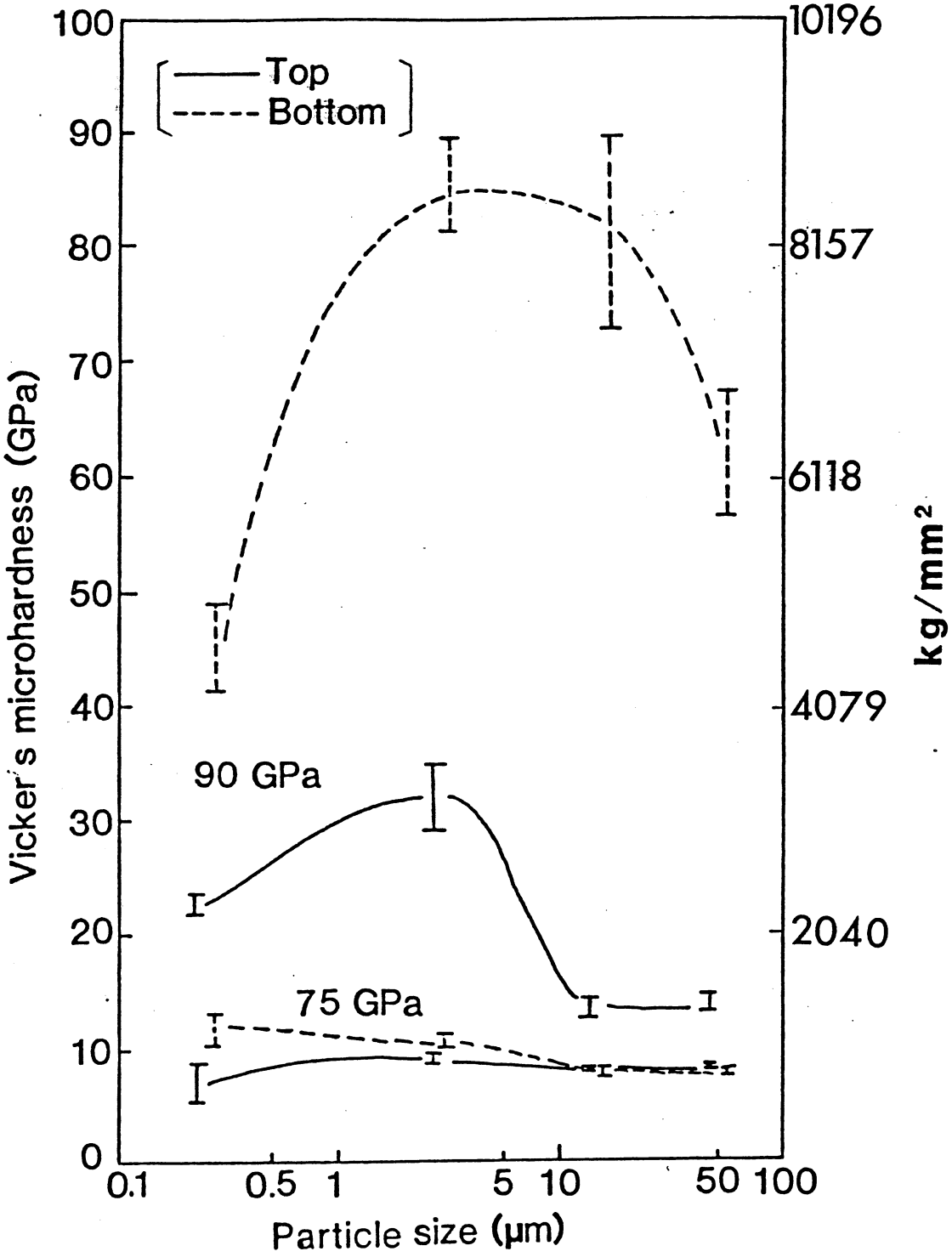

40. Dependence of microhardness of diamond compacts on the starting powder particle size.